

Improvement of near-surface wind speed modeling through refined aerodynamic roughness length in high-roughness surface regions: implementation and validation in the Weather Research and Forecasting (WRF) model version 4.0

Jiamin Wang¹, Kun Yang^{1,2}, Jiarui Liu¹, Xu Zhou³, Xiaogang Ma⁴, Wenjun Tang³, Ling Yuan⁵, Zuhuan Ren¹

¹Ministry of Education Key Laboratory for Earth System Modeling, Department of Earth System Science, Institute for Global Change Studies, Tsinghua University, Beijing 100084, China.

²Renewables Research Center of Huairou Laboratory, Beijing 101499, China.

³National Tibetan Plateau Data Center, State Key Laboratory of Tibetan Plateau Earth System, Environment and Resources, Institute of Tibetan Plateau Research, Chinese Academy of Sciences, Beijing 100101, China.

⁴National Institute of Natural Hazards, Ministry of Emergency Management of China, Beijing, 100085, China.

⁵China State Shipbuilding Corporation Haizhuang Windpower Co., Ltd., Chongqing 401123, China.

Correspondence to: Kun Yang (yangk@tsinghua.edu.cn)

Abstract. Aerodynamic roughness length (z_0) is a key parameter determining near-surface wind profiles, significantly influencing wind-related studies and applications. In high-roughness surface areas, surface roughness has been substantially altered by land use changes such as urbanization. However, many numerical models still assign long-standing and fixed z_0 based on traditional land cover types, neither accounting for shifts in land cover nor updating class-specific z_0 , leaving z_0 values in high-roughness surface regions outdated and unreliable. To address this issue, this study proposed a cost-effective method to estimate z_0 values at weather stations by adjusting z_0 values to minimize the wind speed differences between ERA5 reanalysis data and weather station observation data. Using this approach, z_0 values were derived for 1,837 stations in the high-roughness surface areas across China. Based on these estimates, a high-resolution monthly gridded z_0 dataset was then developed for high-roughness surface areas in China using Random Forest Regression algorithm. Simulations with Weather Research and Forecasting (WRF) model show that implementation of the new z_0 dataset significantly improves the accuracy of 10-m wind speed over high-roughness surface areas, reducing mean wind speed errors by 79.8% and 78.0% compared to the default z_0 in WRF and a latest gridded z_0 dataset from Peng et al. (2022), respectively. Independent validations of 100-m wind speed against anemometer tower data further confirm the dataset's reliability. Therefore, this approach is valuable for wind-dependent studies and applications, such as urban planning, air quality management, and wind energy utilization, by enabling more accurate simulations of wind speed in high-roughness surface areas.

1 Introduction

With the rapid advancement of urbanization and industrialization, human activities and energy use are increasingly concentrated along the settlement-landscape continuum (Liu et al., 2014), particularly in high-roughness areas such as built-

up zones and inhabited vegetated landscapes. High-roughness surface regions not only significantly influence climate change but also are highly sensitive to meteorological and climatic conditions (Kammen and Sunter, 2016). Among various meteorological parameters, wind speed exerts great impacts on both environmental and human systems. One prominent example is that wind speed is a crucial consideration for assessing the atmospheric pollutant dispersion capability (Manju et al., 2002; Han et al., 2017). Specifically, mean flows and atmospheric turbulence are two key factors for pollutant removal (Wong and Liu, 2013; Di Nicola et al., 2022). Also, wind speed regulates pollen dispersion and distribution that are associated with public health (Roy et al., 2023). The utilization of wind energy in high-roughness surface areas also depends on wind speed distribution (Ishugah et al., 2014; Stathopoulos et al., 2018; Tasneem et al., 2020). Proper utilization, through measures such as suburban wind farms or building-integrated turbines, can minimize the need for transmission infrastructure. Beyond energy considerations, wind speed characteristics play a critical role in design and planning of human settlements, influencing both contemporary building practices (Hadavi and Pasdarshahri, 2020) and the preservation of historical-cultural heritage (Li, Y. et al., 2023). Therefore, accurately characterizing wind speed is essential for guiding systematic regulation and promoting sustainable development in high-roughness surface areas.

Aerodynamic roughness length (z_0) is a crucial parameter that determines near-surface wind speed profiles (Stull, 1988). As a key input for atmospheric models, z_0 significantly influences wind speed-related applications, however, its representation in existing numerical models often oversimplifies real-world conditions. Specifically, most models, such as the widely used European Centre for Medium-Range Weather Forecasts Reanalysis v5 (ERA5), determine z_0 with long-standing and fixed values based on traditional land cover types. Such treatment fails to reflect the impact of transitions between surface types and changes in roughness elements within the same type, particularly the complexity of urban structures, thereby posing significant challenges for accurate wind speed simulation and prediction over high-roughness surface areas (Wang et al., 2024). Numerous studies have demonstrated that the changes of z_0 , caused by land use changes, particularly urbanization and industrialization, as well as deforestation and afforestation, significantly impacted wind speed. For instance, the increase in z_0 has explained 70% of the wind speed reduction in Europe (Wever, 2012) and caused a 1.1 m/s decrease in eastern China (Wu et al., 2018). Furthermore, Zhang et al. (2019) identified z_0 changes as a primary driver of long-term wind speed trends in China, Europe, and North America. In line with these findings, Luu et al. (2023) showed that the rise in z_0 , caused by shifts from short vegetation to high vegetation and urbanization, partly contributes to the decline in mean and maximum surface wind speed over Western Europe. A similar mechanism operated in Canada. At Sudbury Airport (Ontario), 10-m wind speeds declined by ~34% during 1975-1995 mainly due to reforestation-induced increases in surface roughness (Tanentzap et al., 2007). These findings highlight the need to refine z_0 in models by incorporating the effects of high-roughness surface areas across urban-town settings and tall-vegetation landscapes. In addition to wind speed, z_0 also plays a significant role in environmental processes. The difference in z_0 between urban and suburban areas is one of drivers causing larger intensity of daytime urban heat islands in humid regions (Zhao et al., 2014; Li et al., 2019). Winckler et al. (2019) showed that roughness changes are a primary control on deforestation's biogeophysical effects, notably surface temperature responses. Therefore, accurate z_0 data in high-roughness surface areas can not only enhance the performance of atmospheric

numerical models, but also provide scientific support for formulating sustainable urban environmental management strategies.

The estimation of z_0 in high-roughness surface areas traditionally relies on three primary approaches: the micrometeorological method, the morphometric method, and a combination of these two methods. The micrometeorological method, based on the Monin-Obukhov similarity theory (Monin and Obukhov, 1954), typically calculates z_0 using observations from flux or anemometer towers (Grimmond et al., 1998; Liu et al., 2018). Although theoretically robust, this method is limited by high costs of instruments and infrastructure (Grimmond and Oke, 1999), as well as the need for homogeneous surface conditions (Wieringa, 1993; Bottema and Mestayer, 1998). The morphometric method usually formulates mathematical models based on geometric characteristics and distribution density of high-roughness surface areas (Raupach, 1992 and 1994; Bottema and Mestayer, 1998; Macdonald et al., 1998; Kanda et al., 2013; Shen et al., 2022; Shen et al., 2024). However, these models often suffer from simplified assumptions and require high-resolution surface feature data, which are costly to acquire (Grimmond and Oke, 1999; Zhang et al., 2017). The combination method, which establishes a relationship between the z_0 ground truth obtained from micrometeorological method and high-resolution surface feature data for regional-scale applications, has shown promise in specific regions, such as Tokyo and Nagoya (Kanda et al., 2013), Beijing (Zhang et al., 2017), and Osaka subregions (Duan and Takemi, 2021). Nevertheless, the limitations of the former two methods hinder its broader applications. Therefore, there is a considerable lack of reliable z_0 data in high-roughness surface regions.

To address the aforementioned challenges, this study proposed a low-cost method for estimating z_0 by integrating 10-m wind speed at China Meteorological Administration (CMA) stations with 10-m wind speed and z_0 from ERA5 reanalysis data. This approach takes advantage of the synergy between CMA's high-density station distribution and ERA5 reanalysis' temporal continuity to substantially enhance the sample size of z_0 estimates. Based on these estimates, we have developed a high-resolution monthly z_0 dataset for high-roughness surface areas in China using Random Forest Regression (RFR) algorithm. The applicability of the new z_0 dataset have been assessed through its implementation in the Weather Research and Forecasting (WRF) model for wind speed simulation. This study contributes to the advancement of mesoscale wind speed simulation over high-roughness surface environments, which can promote wind field-dependent studies, such as urban planning, wind energy utilization, and air quality management.

2 Data and Method

2.1 Data

In this study, we mainly utilized monthly gridded z_0 dataset from ERA5 (Hersbach et al., 2020 and 2023a), referred to as z_{0_ERA5} , along with hourly 10-m wind speed data from both ERA5 (Hersbach et al., 2023b) and surface weather station

97 observations provided by the China Meteorological Administration (CMA) during 2015-2019, to derive z_0 estimates at each
98 CMA station.

99 To extend the site-scale z_0 estimates into a gridded dataset at the regional scale, we applied the RFR algorithm, incorporating
100 six key features: variance of the slope ($\overline{\theta^2}$), terrain standard deviation within 0.01° window (TSD), percent tree cover (PTC),
101 leaf area index (LAI), normalized difference vegetation index ($NDVI$), and urban-rural classification (URC). $\overline{\theta^2}$ was derived
102 as an integral over orographic spectrum, capturing multi-scale orographic complexity with wave length from meter to 10 km
103 (Beljaars et al., 2004). We obtained $\overline{\theta^2}$ from the dataset accompanying the turbulent orographic form drag scheme in WRF
104 (Zhou et al., 2018), which was processed from the global 30" GMTED2010 digital elevation model (Danielson & Gesch,
105 2011). TSD was calculated using elevation data from Shuttle Radar Topography Mission with a spatial resolution of 3
106 arcseconds (Jarvis et al., 2018). The PTC data were obtained from the MOD44B Version 6.1 Vegetation Continuous Fields
107 product (DiMiceli et al., 2022), which provides yearly data at a 250-m pixel resolution. The monthly 1-km $NDVI$ data were
108 acquired from MOD13A3 product (Didan, 2021). The LAI data with an 8-day temporal interval and 500-m spatial resolution
109 were sourced from Yuan et al. (2011) and Lin et al. (2023). URC data were extracted from a 1-km global human settlements
110 map, which categorizes the rural-urban continuum into 19 distinct types (Li, X. et al., 2022 and 2023). To generate a
111 monthly z_0 dataset at a spatial resolution of $0.01^\circ \times 0.01^\circ$, all input datasets were linearly interpolated or resampled to the
112 target resolution. LAI data were averaged monthly by assigning each 8-day interval to the closest month.

113 Additionally, to compare with the existed z_0 datasets, a latest z_0 dataset developed by Peng et al. (2022) (denoted as z_{0_Peng})
114 was used by integrating it into the WRF model for wind speed simulation. This dataset was generated by applying machine
115 learning techniques to integrate FLUXNET ground-based observations and MODIS remote sensing data. Moreover, 100-m
116 wind speed data from 589 anemometer towers in China were utilized for two critical purposes. First, the comparison between
117 tower observations and ERA5 100-m wind speed data (Hersbach et al., 2023b) was used to validate the feasibility of the
118 assumption in the z_0 estimation method. Second, tower data were used as independent validations to evaluate the impact of
119 refined z_0 on wind speed simulations. These anemometer towers cover varying periods between 2004 and 2022 with a
120 temporal resolution of 10 min.

121 2.2 Method for deriving z_0 at CMA stations

122 First, the theoretical basis for deriving z_0 at CMA stations is presented. In the framework of Monin-Obukhov similarity
123 theory (Monin and Obukhov, 1954), the neutral logarithmic wind profile can be expressed with Equation (1).

$$124 \quad u_z = \frac{u_*}{k} \ln \left(\frac{z - d}{z_0} \right) \quad (1)$$

125 where u_z is the wind speed (m/s) at height z , the measuring height above ground (m); u_* is the friction velocity (m/s); k is
126 the von Karman constant and equals to 0.4, and d is the zero-plane displacement height (m), calculated as $d = 20/3 z_0$ using
127 a widely accepted empirical formula (Watts et al., 2000).

128 Based on Equation (1), the 100-m neutral wind speed for ERA5 and CMA stations can be expressed in Equations (2) and (3),
 129 respectively.

$$130 \quad u_{100_ERA5} = u_{10_ERA5} \frac{\ln\left(\frac{100 - d_{ERA5}}{z_{0_ERA5}}\right)}{\ln\left(\frac{10 - d_{ERA5}}{z_{0_ERA5}}\right)} \quad (2)$$

$$131 \quad u_{100_CMA} = u_{10_CMA} \frac{\ln\left(\frac{100 - d_{CMA}}{z_{0_CMA}}\right)}{\ln\left(\frac{10 - d_{CMA}}{z_{0_CMA}}\right)} \quad (3)$$

132 And then z_0 values at CMA stations can be estimated by the following three steps:

133 First, we assumed: (1) the near-surface wind speed difference between ERA5 and CMA is primarily attributed to z_0 , and the
 134 influence of z_0 diminishes with height. Consequently, the 100-m wind speed from ERA5 reanalysis is considered
 135 comparable to that from observations; (2) the impact of atmospheric stability on wind speed is identical for both ERA5 and
 136 CMA stations, allowing us to neglect stability correction terms under non-neutral conditions when deriving z_0 for each
 137 hourly interval. The validity of these assumptions will be supported by the subsequent validation of wind speed simulations
 138 based on the derived z_0 values (Section 3.3).

139 Second, we calculated the hourly z_{0_CMA} values based on Equations (2) and (3). Given that u_{10_ERA5} , u_{10_CMA} , and z_{0_ERA5}
 140 values are known, an optimal z_{0_CMA} value at each hour was derived through minimizing the difference between u_{100_ERA5}
 141 and u_{100_CMA} calculated using Equations (2) and (3). To align with Assumption (1), we only retained z_{0_CMA} values
 142 corresponding to times when the percentage difference between the calculated u_{100_ERA5} and u_{100_CMA} was less than 10%.
 143 ERA5 provides native 100-m winds, but here we use log-law–reconstructed 100-m winds from u_{10_ERA5} and z_{0_ERA5} instead.
 144 The reason is that the z_{0_CMA} is derived under the assumption that stability-correction term is neglected. This means that the
 145 100-m wind speeds in Equations (2) and (3) are both calculated without considering stability effects. However, the native
 146 ERA5 100-m wind field inherently embeds model-diagnosed stability influences. Therefore, directly pairing native ERA5
 147 100-m winds with our CMA log-law construction would amplify the error in the derived $\ln(z_0)$. In addition, the
 148 reconstruction offers two practical advantages. First, it requires fewer variables and a more transparent linkage, relying only
 149 on 10-m wind speeds and z_0 from reanalysis, together with 10-m wind speeds from observations; Second, our results
 150 indicate that the z_0 estimates are not particularly sensitive to the choice of reference height (see Section 4. Discussion), so
 151 there is no need to use native reanalysis winds at heights other than 10 m.

152 Third, these retained z_{0_CMA} values were grouped by months, and the monthly median values were selected as the final
 153 roughness length ($z_{0_optimal}$). To avoid unreasonable estimates, the values of $z_{0_optimal}$ satisfying the condition that the
 154 absolute difference between $\ln(z_{0_optimal})$ and the corresponding $\ln(z_{0_ERA5})$ does not exceed 2 were considered valid.

155 Finally, we obtained monthly z_0 estimates at 1,837 stations out of the 2,161 CMA stations.

156 2.3 Method for estimating gridded z_0 at regional scale

157 Machine learning serves as an effective tool for extending the $z_{0_optimal}$ estimates at CMA stations to the regional scale. In
158 this study, we employed the RFR algorithm (Equation (4)) (Breiman, 2001), a widely used method for similar applications
159 (Duan and Takemi, 2021; Hu et al., 2022; Peng et al., 2022 and 2023). All samples were divided into training and test
160 subsets at a ratio of 8:2 for each bin of $\ln(z_{0_optimal})$, with the bins defined at intervals of 0.2. Sensitivity tests were
161 conducted to determine the optimal number of decision trees in the RFR algorithm (Fig. 3b), resulting in the selection of 300
162 trees. The maximum depth of the trees was set to 18, and the minimum sample split was set to 5. Five-fold cross-validation
163 shows the stable performance (Fig. 3d). Furthermore, the training and test results exhibit minimal sensitivity to the
164 randomization seed used for dataset splitting (Fig. 3a). The resulting gridded aerodynamic roughness length data are referred
165 to as z_{0_RFR} .

$$166 \quad \ln(z_0) = f(\theta^2, TSD, PTC, LAI, NDVI, URC, month) \quad (4)$$

167 2.4 Model configuration

168 To demonstrate the applicability of gridded z_{0_RFR} data, the WRF (Version 4.0) Model (Skamarock et al., 2019) was used in
169 this study to simulate wind speed with z_{0_RFR} . For comparison, two additional simulations were performed: one utilized the
170 WRF model's default roughness length ($z_{0_Default}$) based on land cover types, and the other used z_{0_Peng} .
171 First, we set z_{0_RFR} and z_{0_Peng} in WRF model, respectively. Given that z_{0_RFR} is concentrated in high-roughness surface
172 areas, the missing values over other regions are filled with $z_{0_Default}$. Notably, the setting of z_{0_Peng} in WRF is different
173 from that of z_{0_RFR} . In the WRF model, z_0 values over bare fraction and vegetated fraction are determined separately.
174 Specifically, in the Noah-MP land surface model, z_0 is set to a constant over bare areas, while it is assigned by a look-up
175 table according to vegetation type over vegetated areas. Peng et al. (2022) only provided the z_0 over vegetation areas, which
176 is the gridded mean effective roughness length including vegetated fraction and bare fraction. Thus, before conducting the
177 simulation of wind speed in the WRF model with the gridded z_{0_Peng} , we adjusted the roughness length over vegetated
178 fraction in each grid from z_{0_Peng} . The specific adjustment of z_{0_Peng} in the WRF model is comprehensively described in the
179 supplementary material Section 1. Apart from the difference in the sources of z_0 , other model configurations for z_{0_RFR} ,
180 $z_{0_Default}$, and z_{0_Peng} are identical. The specific model configurations are as follows.
181 The simulation domains were configured with a “lat-lon” map projection, centered at coordinates 31.5°N, 109.0°E. As
182 illustrated in Fig. 4b, nested domains were employed, with horizontal resolutions of 0.09° for Domain 1 (d01) and 0.03° for
183 Domain 2 (d02). Specifically, d01 consisted of 225 grid points in the west-east direction and 191 in the south-north direction,
184 while d02 consisted of 469 grid points in the west-east direction and 367 in the south-north direction. The vertical level had
185 70 layers and was stretched with $dzstretch_s = 1.1$ and $dzstretch_u = 1.04$. The model top was set to 50 hPa. The
186 simulation periods spanned from March 31st to April 30th in 2019. The integral time interval was set to 30 seconds. The re-

187 initialization simulation was performed. Specifically, each simulation started at 12:00 local time (LT, LT=UTC+8) and ran
 188 for 36 hours until 24:00 LT the next day. The first 12 hours were considered the spin-up time and the remaining hours were
 189 used for analysis. Additionally, the initial and boundary conditions in the simulations were taken from hourly ERA5
 190 reanalysis data, which provide pressure-level variables (geopotential height, air temperature, air humidity, and wind field)
 191 (Hersbach et al., 2023c) and surface variables (surface air temperature, humidity, pressure, 10 m wind field, sea level
 192 pressure, land surface temperature, soil temperature, and soil water content) (Hersbach et al., 2023b).
 193 For physical parameterization schemes, the modified Thompson microphysics scheme (Thompson et al., 2008), Dudhia
 194 scheme for shortwave radiation (Dudhia, 1989), Rapid Radiative Transfer Model (RRTM) scheme for longwave radiation
 195 (Mlawer et al., 1997), Noah-MP land surface model (Niu et al., 2011), Yonsei University scheme for planetary boundary
 196 layer (Hong et al., 2006), and Grell-Freitas for cumulus parameterization (Grell and Freitas, 2013) were adopted. The
 197 cumulus parameterization scheme was activated only in the d01 domain and switched off in the d02 domain. A turbulent
 198 orographic form drag scheme with description of the dynamic drag caused by sub-grid orography was also applied (Beljaars
 199 et al., 2004; Zhou et al., 2018).

200 2.5 Calculation of statistical metrics

201 To evaluate the performance of the simulated wind speed with z_{0_RFR} , $z_{0_Default}$, and z_{0_Peng} , three statistical metrics,
 202 including correlation coefficient (R), mean absolute bias (MAB), and root mean square error ($RMSE$), were used in temporal
 203 and spatial aspects. For the spatial performance assessment, the average 10-m wind speed simulation during April 1st to 30th
 204 in 2019 at each station was used to calculate R , MAB , and $RMSE$ with the CMA observations.
 205 Regarding the temporal evaluation, the *index* (representing R , MAB , and $RMSE$) was calculated as the mean of the
 206 corresponding metric for hourly 10-m wind speed during April 1st to 30th in 2019 across all CMA stations (Equation (5)).

$$207 \quad index = \frac{\sum_{i=1}^M index_i}{M} \quad (5)$$

208 where $index_i$ denotes the respective metric value at the i -th station, and M represents the total number of stations.
 209 Additionally, to incorporate the direction of the bias into the wind-speed evaluation, we used the mean bias percentage (MBP)
 210 to quantify the signed bias of ERA5 reanalysis and simulated wind speeds against observations from CMA stations and
 211 anemometer towers (Equation (6)).

$$212 \quad MBP = \frac{\bar{u}_{sim} - \bar{u}_{obs}}{\bar{u}_{obs}} \times 100\% \quad (6)$$

213 where \bar{u}_{sim} represents mean wind speed from ERA5 or model simulations, and \bar{u}_{obs} represents observed mean wind speed
 214 from CMA stations and anemometer towers.

215 To more intuitively compare the performance of wind speed simulations using $z_{0_Default}$, z_{0_Peng} , and z_{0_RFR} , we also
 216 calculated the percentage reduction in wind speed error (PRE) achieved by z_{0_RFR} relative to $z_{0_Default}$ and z_{0_Peng}
 217 (Equation (7)).

$$218 \quad PRE = \frac{|\bar{u}_{z_{0_*}} - \bar{u}_{observation}| - |\bar{u}_{z_{0_RFR}} - \bar{u}_{observation}|}{|\bar{u}_{z_{0_*}} - \bar{u}_{observation}|} \times 100\% \quad (7)$$

219 where $\bar{u}_{z_{0_*}}$ represents $\bar{u}_{z_{0_Default}}$ or $\bar{u}_{z_{0_Peng}}$, and \bar{u} denotes the mean 10-m or 100-m wind speed from simulations based on
 220 $z_{0_Default}$, z_{0_Peng} , and z_{0_RFR} , as well as from observations (CMA stations or anemometer towers).

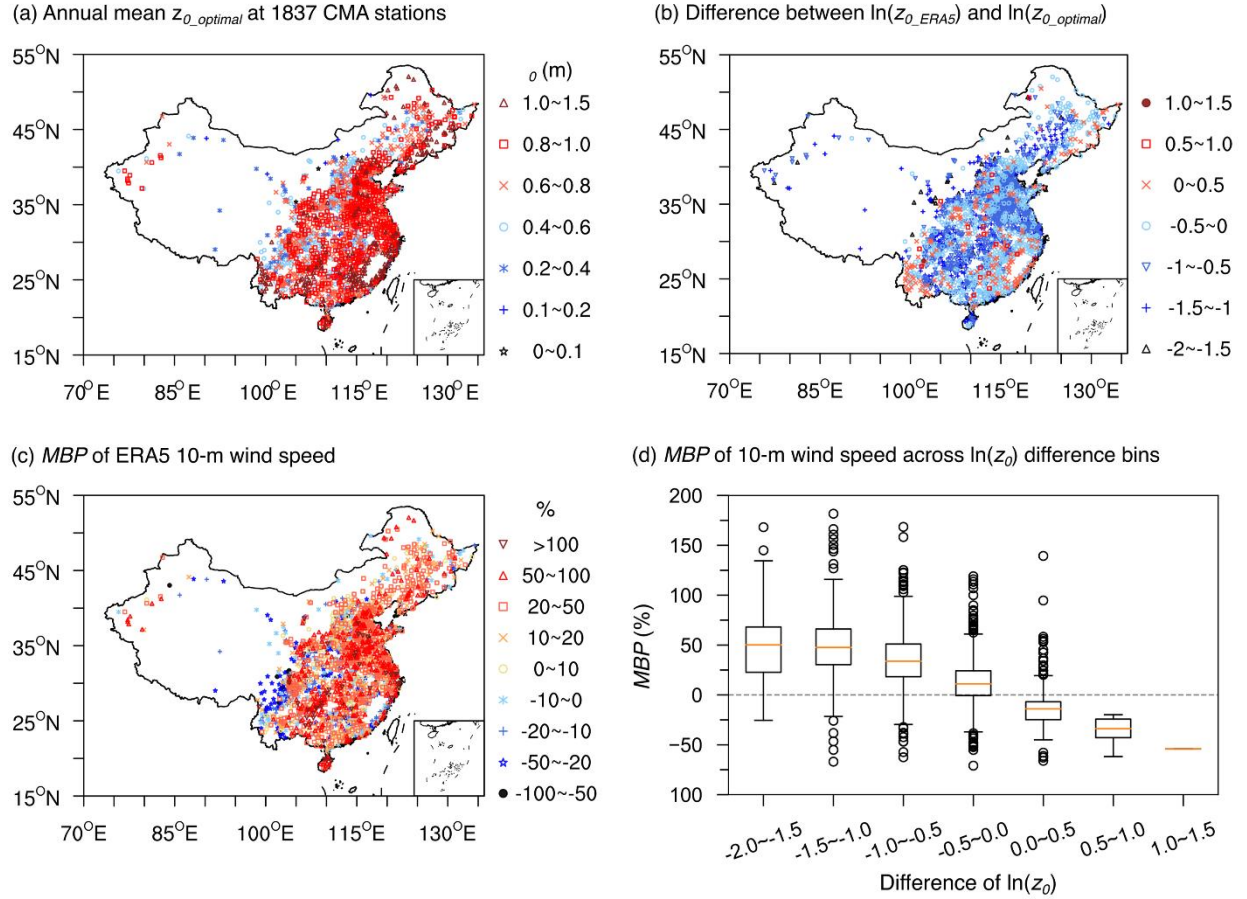
221 3 Results

222 3.1 The distribution characteristics of the z_0 estimates at CMA stations

223 Figure 1a presents the spatial distribution of annual mean $z_{0_optimal}$ values derived from 1,837 CMA stations, representing a
 224 subset of all accessible 2,161 stations (Fig. S1a). These 1,837 stations are primarily located in the eastern, southern, and
 225 central regions of China, with most stations having z_0 values ranging between 0.2 and 1.5 m. In contrast, the excluded 324
 226 stations are mostly distributed in the western regions of China. The exclusions of these stations can be attributed to the poor
 227 performance of ERA5 100-m wind speed data, which may result from altitude differences between the observation sites and
 228 the model terrain, thereby rendering our initial assumption, i.e. ERA5 100-m wind speed data are reliable for z_0 estimation,
 229 invalid in these areas. To test this, we evaluated the performance of ERA5 100-m wind speed by comparing it with 589
 230 anemometer tower data, since CMA stations only provide 10-m wind speed observations. Overall, ERA5 shows a smaller
 231 MBP in the eastern regions compared to the western regions (Fig. 2a). Therefore, the spatial distribution of the 1,837 stations
 232 with valid z_0 values is reasonable.

233 Additionally, as a consistency check, we examined how the difference in $\ln(z_0)$ covaries with the 10-m wind-speed bias
 234 between ERA5 reanalysis and station observations. Compared to the annual mean $\ln(z_{0_optimal})$ derived from 1,837 stations,
 235 the $\ln(z_{0_ERA5})$ values are systematically lower at most locations, resulting in positive MBP values of 10-m wind speed
 236 between ERA5 reanalysis data and station observations (Figs. 1b and 1c). The discrepancies between $\ln(z_{0_ERA5})$ and
 237 $\ln(z_{0_optimal})$ are likely due to rapid urbanization around the majority of CMA stations, characterized by extensive
 238 construction of buildings, which enhances surface roughness and consequently reduces near-surface wind speeds (Li et al.,
 239 2018; Zhang and Wang, 2021). However, the impact of urbanization is likely not considered in the ERA5 reanalysis. Figures
 240 2b and 2c depict the distribution of CMA stations classified by urban-rural categories. All stations are situated in high-
 241 roughness surface areas, with the majority located in urban and town regions, highlighting the need to incorporate
 242 urbanization effects into wind speed simulations to improve model accuracy. In contrast, at a few locations, where the
 243 $\ln(z_{0_ERA5})$ values are higher, the corresponding MBP values of 10-m wind speed are negative (Figs. 1b and 1c). The

244 influence of $\ln(z_0)$ difference on wind speed bias becomes more pronounced as the magnitude of $\ln(z_0)$ deviation increases
 245 (Fig. 1d). Because $\ln(z_{0_optimal})$ is defined as a monthly median of hourly $\ln(z_0)$, this cross-time statistic does not trivially
 246 inherit the instantaneous relationship implied by Equations (1)-(3). The monotonic, theory-consistent pattern observed in the
 247 binned $\ln(z_0)$ difference versus wind-speed *MBP* therefore serves as a post-aggregation consistency check, rather than as
 248 proof. Accordingly, the robust consistency in the relationship between z_0 and wind speed preliminarily supports that
 249 $z_{0_optimal}$ is reasonable, and suggests that improving z_0 values over high-roughness surface areas in numerical models could
 250 significantly enhance wind speed simulation accuracy. The validity of $z_{0_optimal}$ will be assessed via independent validation
 251 by comparing simulated wind speeds with observations (Section 3.3).



252
 253 **Figure 1.** (a) Spatial distribution of annual mean $z_{0_optimal}$ across 1,837 CMA stations. (b) Difference between annual mean $\ln(z_{0_ERA5})$
 254 and $\ln(z_{0_optimal})$ (i.e., $\ln(z_{0_ERA5})$ minus $\ln(z_{0_optimal})$). (c) *MBP* of 10-m wind speed between ERA5 and CMA stations. (d) Boxplots
 255 illustrating the statistical distribution of the *MBP* for 10-m wind speed shown in (c) across different intervals of $\ln(z_0)$ difference shown in
 256 (b).

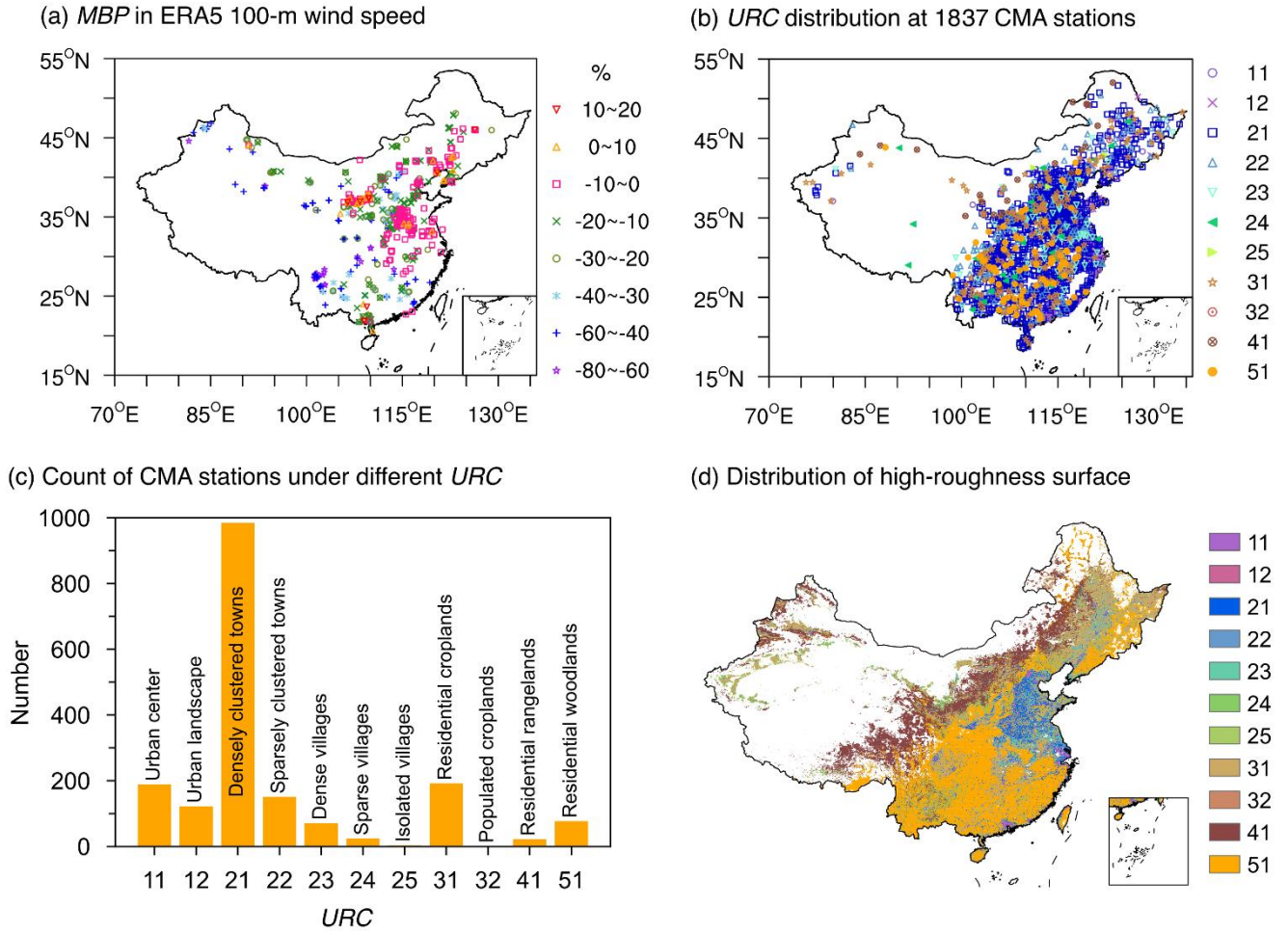


Figure 2. (a) *MBP* of 100-m wind speed between ERA5 and 589 anemometer towers. (b) Spatial distribution of urban-rural classification (*URC*) at 1,837 CMA stations. The legend on the right indicates the *URC* codes, with the corresponding *URC* types labeled in panel (c). (c) Number of CMA stations for each *URC*. The numerical labels on the x-axis represent the *URC* codes, with the specific *URC* types annotated on the bars. (d) Spatial distribution of high-roughness surface areas, which are composed of the 11 types covered by CMA stations in panel (b).

3.2 Development of a gridded z_0 dataset in high-roughness surface areas across China

To demonstrate the reliability and practicality of the estimated $z_{0_optimal}$, we constructed a gridded z_0 dataset based on these estimations in order to apply it in numerical simulations. Given that the estimated z_0 values from 1,837 stations are located within high-roughness surface areas consisting of 11 distinct types (Figs. 2b and 2c), this study developed a monthly gridded z_0 dataset specifically for these categories of areas with a spatial resolution of $0.01^\circ \times 0.01^\circ$ using the RFR algorithm, referred to as z_{0_RFR} . As a representative example, the z_{0_RFR} dataset was generated for the year 2019, and its spatial

269 coverage is shown in Fig. 2d. Although 2019 was chosen for demonstration, the RFR model itself is year-independent and
 270 can be applied to other years, provided that the required input features are available. Six feature variables closely related to
 271 z_0 were used as inputs, encompassing topographic characteristics ($\overline{\theta^2}$ and TSD), vegetation conditions (PTC , LAI , and $NDVI$),
 272 and urban-rural distribution (URC).
 273 Figure 3c shows that the RFR algorithm exhibits satisfactory performance on both training and test subsets. Feature
 274 importance analysis reveals that topographic features and PTC exert the most significant influence on $\ln(z_{0_RFR})$ (Fig. 3e).
 275 z_0 is primarily controlled by the characteristic height of surface roughness elements, particularly their relief. Consequently,
 276 topographic features rank among the most influential factors. For vegetation-related features, PTC not only reflects the
 277 horizontal distribution of vegetation density but also serves as a proxy for the presence of tall roughness elements. By
 278 contrast, LAI mainly represents vegetation density, making it relatively less critical. Although LAI is strongly correlated with
 279 $NDVI$ ($R = 0.72$), its low importance is not driven by this collinearity. The URC ranks only fourth in feature importance.
 280 This ranking should not be interpreted as implying that land use or urbanization is insignificant. Rather, in our framework,
 281 URC is used mainly to delineate the study domain and to ensure that the RFR algorithm is applied only to high-roughness
 282 surface areas. The aerodynamic effects of high-roughness elements, such as tall vegetation, buildings, and other
 283 infrastructure, are already embedded in the wind observations from CMA stations. As a result, the influence of these
 284 roughness elements is directly reflected in the z_0 values themselves, rather than being captured by the URC . Essentially,
 285 URC is not defined in terms of the morphological height and density of roughness elements; instead, it is derived from global
 286 land-cover and population data (Li, X. et al., 2023), and is therefore weakly sensitive to z_0 . For example, in categories of
 287 Urban center and Urban landscape, there remains non-negligible tree cover, mean tree fractions of approximately 10% and
 288 11%, respectively (Fig. S1b). This lowers URC 's ranking in feature-importance analyses. To better capture the influence of
 289 roughness elements, more detailed surface parameters, such as building height and building density, would be helpful. Once
 290 such data are widely accessible, they should be incorporated to further improve the accuracy of z_0 estimates.

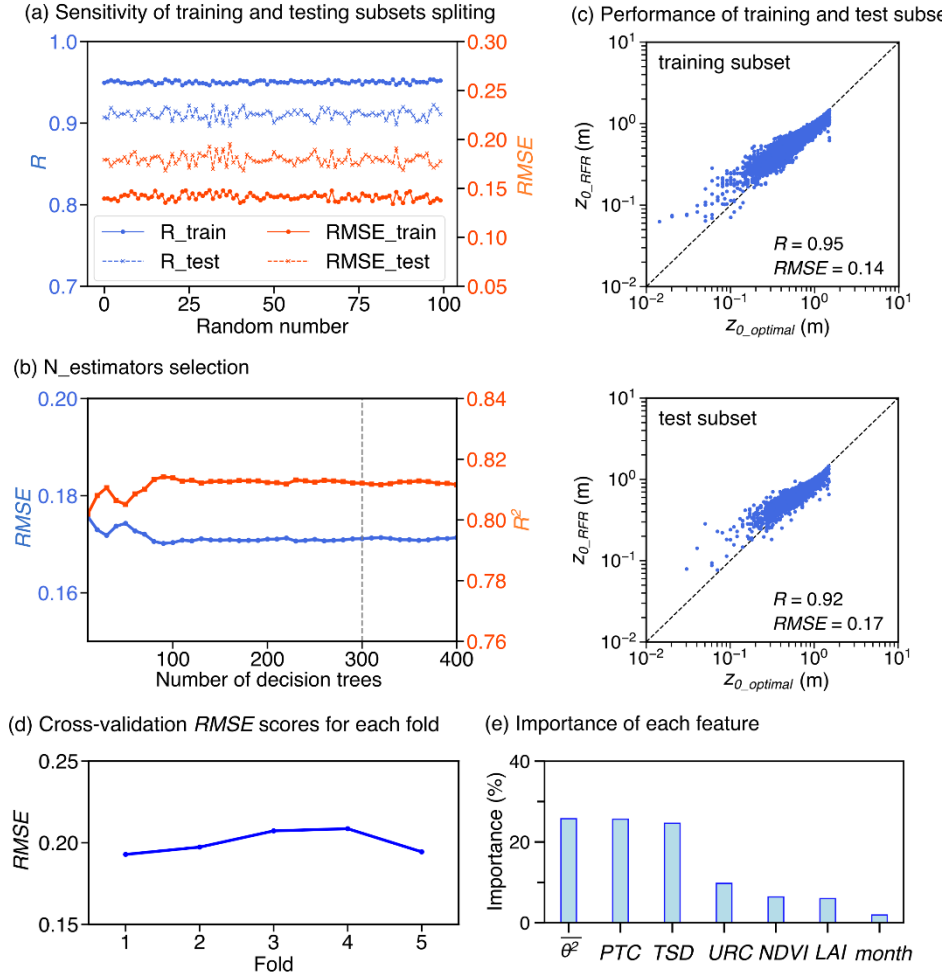
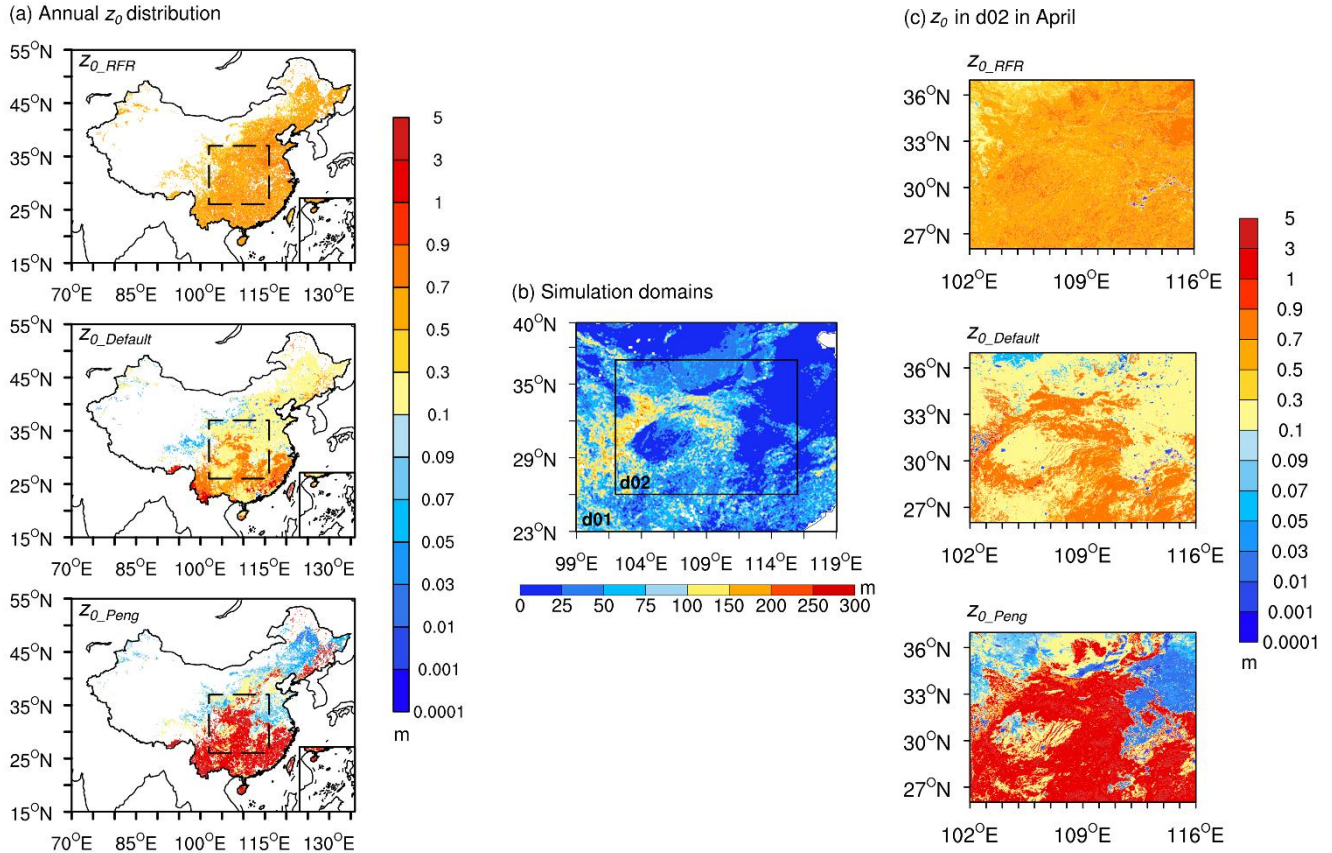


Figure 3. Sensitivity analysis and performance evaluation of the Random Forest Regression (RFR) algorithm. (a) Sensitivity of RFR results to the randomization seed for training and test subsets splitting. R and $RMSE$ represent correlation coefficient and root mean square error, respectively. (b) Determination of the optimal number of decision trees. R^2 represents determination coefficient. (c) Performance of the RFR algorithm on the training and test subsets. The R and $RMSE$ values are displayed. (d) Performance evaluation using five-fold cross-validation. (e) Importance scores of different feature variables.

The spatial distribution of $\ln(z_{0_RFR})$ shows limited monthly variability (Fig. S2). The most pronounced monthly variations occur predominantly in the northern regions, likely because these areas exhibit strong seasonal changes in vegetation structure and biomass. The annual mean spatial distribution of z_{0_RFR} , with values in high-roughness surface areas generally falling within the range of 0.3 to 0.9 m, exhibits distinct patterns compared to $z_{0_Default}$ and z_{0_Peng} (Fig. 4a). In comparison with $z_{0_Default}$ and z_{0_Peng} , z_{0_RFR} shows a more homogeneous spatial distribution pattern across China. Specifically, in northern China, z_{0_RFR} values are consistently higher than those of both $z_{0_Default}$ and z_{0_Peng} , with $z_{0_Default}$ generally

304 higher than z_{0_Peng} . Conversely, in southern China, z_{0_Peng} values are significantly higher than both $z_{0_Default}$ and z_{0_RFR} .
 305 However, in southeastern and southwestern China, $z_{0_Default}$ values exceed those of z_{0_RFR} , while in the remaining southern
 306 areas, z_{0_RFR} maintains higher values compared to $z_{0_Default}$.



307
 308 **Figure 4.** (a) Spatial distributions of annual mean z_{0_RFR} , $z_{0_Default}$, and z_{0_Peng} . The dashed rectangular box indicates the simulation
 309 domain (d02) in panel (b). (b) Nested simulation domains (d01: outer domain; d02: inner domain) with terrain standard deviation within
 310 0.01° window (TSD) represented by color shading. (c) Spatial distributions of z_0 used in simulations over d02 in April.

311 3.3 Application of the produced z_0 datasets in wind speed simulation

312 To evaluate the performance of z_{0_RFR} , we implemented it in the WRF model for wind speed simulations, as z_0 directly
 313 affects near-surface wind speed. A 3-km simulation for April 2019 was conducted using the WRF model with z_{0_RFR} over
 314 the regions outlined in Fig. 4a, which correspond to the d02 domain in Fig. 4b and represent the primary areas of z_{0_RFR}
 315 concentration. April was selected because it is the month with the highest average wind speed in the target domain (Fig. S3),
 316 thus better reflecting the impact of z_0 on wind speed. For comparison, two additional simulations were performed: one

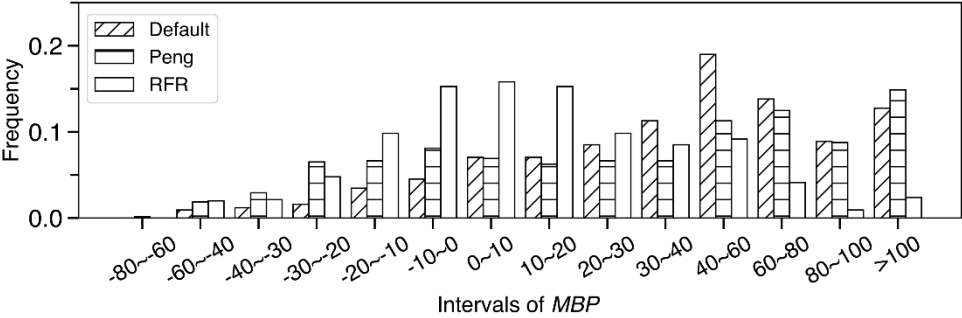
utilizing the WRF model's default roughness length ($z_{0_Default}$) based on land cover types, and the other employing a recent z_0 dataset (z_{0_Peng}). In the northeastern, northern, and western regions of the d02 domain, both $z_{0_Default}$ and z_{0_Peng} are generally lower than z_{0_RFR} estimates, with z_{0_Peng} having even lower values than $z_{0_Default}$ (Fig. 4c). However, this pattern reverses in the southeastern areas and along the surrounding area of the Sichuan Basin, where both $z_{0_Default}$ and z_{0_Peng} surpass z_{0_RFR} estimates, and notably, with z_{0_Peng} having significantly higher values than $z_{0_Default}$ in these regions. These discrepancies in z_0 would inevitably directly affect the accuracy of wind speed simulation. To evaluate the influence, we conducted a comprehensive assessment on both 10-m and 100-m wind speed simulations, which represent typical heights for meteorological observations and wind energy applications, respectively.

3.3.1 Evaluation of the simulated 10-m wind speed

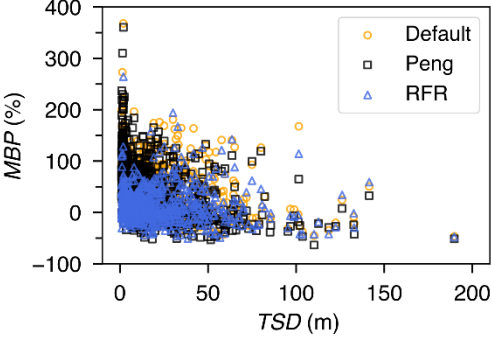
We first compared the simulated 10-m wind speed with observations from 753 CMA stations in study areas (d02 domain), showing that z_{0_RFR} significantly enhances the accuracy of simulations. The improvement due to z_{0_RFR} is evident in the smaller MBP values of the simulated wind speed (Figs. 5a and S4) and the closer alignment of average wind speed with observational data (Fig. 6a). Specifically, the frequency histogram of MBP values reveals that the simulation results using z_{0_RFR} mostly fall within an absolute MBP range of less than 30%, with a substantial proportion concentrated below 10%. In contrast, simulations employing $z_{0_Default}$ display a majority of MBP values exceeding 30%, while simulations using z_{0_Peng} are even poorer, with a larger number of stations falling within higher MBP ranges (Fig. 5a). The improvement in 10-m wind speed induced by z_{0_RFR} is primarily evident in relatively flat regions. As TSD increases, the improvement gradually diminishes (Fig. 5b). z_{0_RFR} outperforms both $z_{0_Default}$ and z_{0_Peng} when TSD does not exceed 50 m, while it shows superior performance to $z_{0_Default}$ and comparable results to z_{0_Peng} when TSD is greater than 50 m (Fig. 5c). Spatially, significant improvements are observed in the relatively flat eastern and northern study areas, whereas limited enhancements are found in regions with higher TSD surrounding the Sichuan Basin (Fig. S4). The limited improvement in relatively complex terrain arises because, in addition to z_0 , wind speed over these regions is influenced by multi-scale factors, including microscale terrain features (Ge et al., 2025), turbulent orographic form drags (Beljaars et al., 2004; Jiménez and Dudhia, 2011; Zhou et al., 2018), surface heating-induced mountain-valley circulations (Kim et al., 2021), mountain waves (Draxl, et al., 2021) and other processes. Inaccurate parameterizations of these factors in numerical models can all lead to errors in wind speed simulations. For the mean 10-m wind speed, simulations using z_{0_RFR} (2.26 m/s) show better agreement with the CMA observations (2.08 m/s), whereas simulations with $z_{0_Default}$ and z_{0_Peng} show greater overestimations, producing mean wind speeds of 2.97 m/s and 2.90 m/s, respectively (Fig. 6a and Table 1). In other words, z_{0_RFR} decreases mean bias of 10-m wind speed by 79.8% and 78.0% compared to $z_{0_Default}$ and z_{0_Peng} , respectively. Independent validations across 148 stations (Fig. 6b), from the test subset in the generation of z_{0_RFR} , further confirm the superiority of z_{0_RFR} (Fig. 6a). In addition, the improvements in

348 10-m wind speed were observed throughout the entire simulation period (Fig. 6c). Note that our experimental design,
 349 employing a re-initialization strategy, means that 30 independent simulation experiments were conducted in April. Thus,
 350 although the simulations were only conducted for a month, the consistent improvement across all days shows that the
 351 enhancement achieved by z_{0_RFR} is robust. Moreover, the statistical metrics also show that the simulated 10-m wind speed
 352 using z_{0_RFR} outperforms those using $z_{0_Default}$ and z_{0_Peng} in temporal *MAB* and *RMSE* (Fig. 6d).

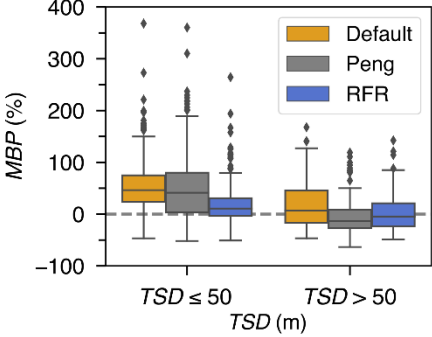
(a) Frequency of MBP intervals in simulated 10-m wind speed



(b) MBP of 10-m wind speed distribution over TSD



(c) MBP of 10-m wind speed for TSD categories



353
 354 **Figure 5.** (a) Frequency distribution of *MBP* in simulated 10-m wind speed in April using $z_{0_Default}$, z_{0_Peng} , and z_{0_RFR} against
 355 observations from CMA stations. (b) Distribution of *MBP* in 10-m wind speed as a function of *TSD*. (c) Box plot of *MBP* in 10-m wind
 356 speed across different *TSD* bins.

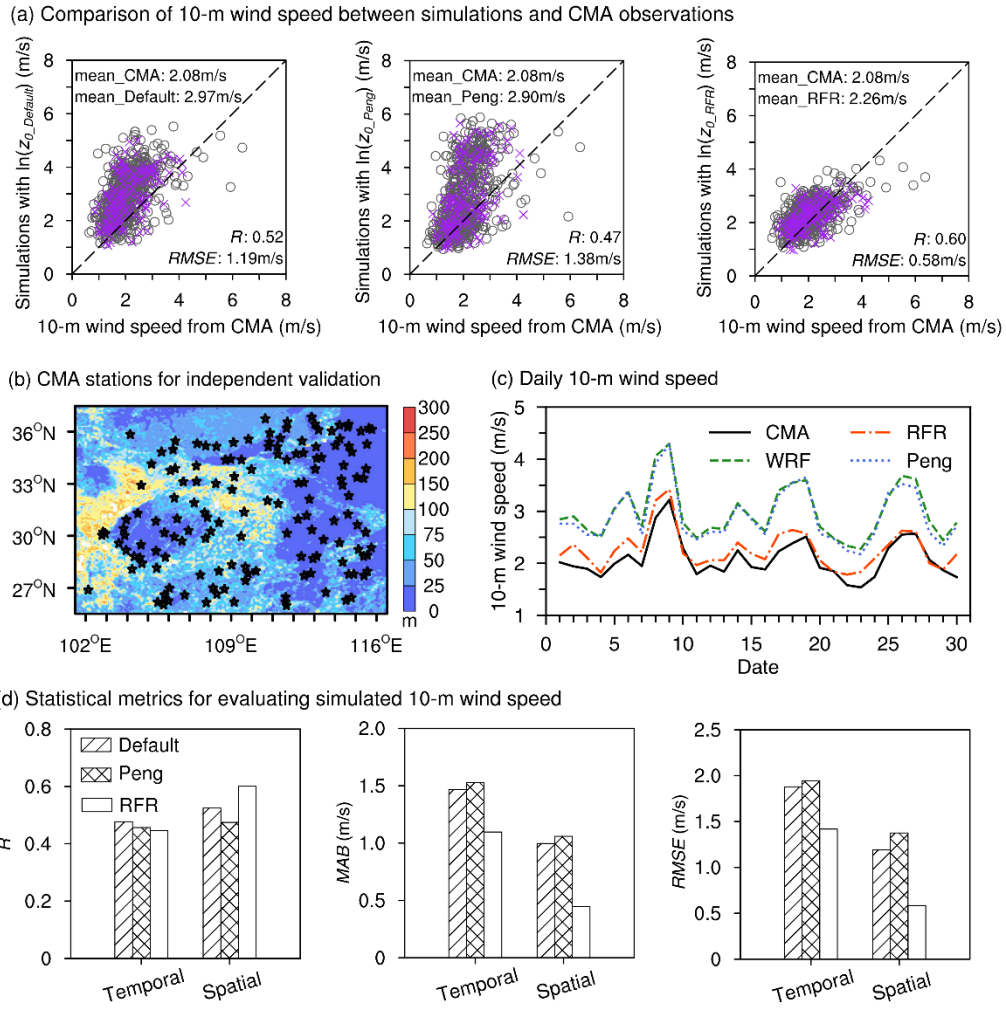


Figure 6. (a) Comparisons of mean 10-m wind speed in April between the simulations using $z_{0_Default}$, z_{0_Peng} , and z_{0_RFR} versus observations from CMA stations. All points (grey circles and purple crosses) represent the 753 CMA stations within the d02 domain available for comparison, while the purple crosses represent the 148 stations utilized for independent validation, which were not used in training the z_{0_RFR} model. The corresponding wind speed means, R , and $RMSE$ of all stations are also indicated. (b) Distribution of the 148 independent CMA stations (black stars). Colored shaded areas represent TSD . (c) Comparison of daily mean 10-m wind speed between simulations and observations from 753 CMA stations. (d) Statistical metrics comparing simulated and observed 10-m wind speeds, including temporal and spatial R , MAB , and $RMSE$.

Table 1. Mean 10-m wind speed at 753 CMA stations and mean 100-m wind speed at 50 anemometer towers from simulations and observations. Simulations were performed using $z_{0_Default}$, z_{0_Peng} , and z_{0_RFR} . Also shown is the percentage reduction in wind speed error (PRE) achieved by z_{0_RFR} relative to $z_{0_Default}$ and z_{0_Peng} .

	$z_{0_Default}$	z_{0_Peng}	z_{0_RFR}	Observations
--	------------------	---------------	--------------	--------------

Mean 10-m wind speed (m/s)	2.97	2.90	2.26	2.08
<i>PRE</i> in 10-m wind speed (%)	79.8%	78.0%	-	-
Mean 100-m wind speed (m/s)	7.09	7.29	6.50	6.26
<i>PRE</i> in 100-m wind speed (%)	71.1%	76.7%	-	-

369 3.3.2 Evaluation of the simulated 100-m wind speeds

370 In addition to 10-m wind speed, the simulated 100-m wind speed was also improved through the use of z_{0_RFR} (Fig. 7a and
371 Table 1). Compared to observations from 50 anemometer towers (Fig. 7b), with an average 100-m wind speed of 6.26 m/s,
372 simulations based on $z_{0_Default}$ and z_{0_Peng} overestimate the wind speed, with averages of 7.09 m/s and 7.29 m/s,
373 respectively. However, the mean 100-m wind speed simulated using z_{0_RFR} is 6.50 m/s, closer to the observations (Table 1).
374 This improvement using z_{0_RFR} reduces wind speed mean bias by 71.1% and 76.7% compared to $z_{0_Default}$ and z_{0_Peng} ,
375 respectively. Consistent with the performance of z_{0_RFR} at 10-m wind speed, the improvement in 100-m wind speed is more
376 pronounced in relatively flat regions (Fig. 7c). The outliers in Fig. 7a, where wind speed biases remain significant despite
377 using z_{0_RFR} , are located in areas with higher *TSD*. Furthermore, similar to its performance at 10-m height, z_{0_RFR}
378 demonstrates superior performance in simulated 100-m wind speed across both temporal and spatial metrics, with the
379 exception of the temporal correlation coefficient (Fig. 7d). The relatively lower temporal *R* is reasonable, as the
380 improvement in wind speed induced by z_0 primarily stems from enhancements in the vertical profile.

381 In summary, the 30 independent simulation cases conducted for April demonstrate that the z_0 values derived from the
382 combination of CMA observations and ERA5 data are highly reliable. The resulting gridded z_0 dataset significantly reduces
383 uncertainties in mesoscale near-surface wind speed simulations, particularly over relatively flat high-roughness surface areas.
384 To further validate the robustness of the z_0 estimation method and the resulting dataset, we conducted additional simulations
385 for October 2019, a month characterized by generally weaker wind conditions (Fig. S3), using the same model configuration
386 as in April. The results (Figs. S5-S7) also show consistent improvements when using z_{0_RFR} . Station-wise correlations
387 increase and errors decrease to a similar extent in both months, and the daily time series likewise show closer tracking of
388 peaks and lulls. Taken together, these results further reinforce the reliability and applicability of the proposed z_0 estimation
389 under varying meteorological conditions. They also indicate that although phenology-driven changes in canopy structure and
390 seasonal circulation modulate wind speeds, the performance advantage of the proposed z_0 is not diminished.

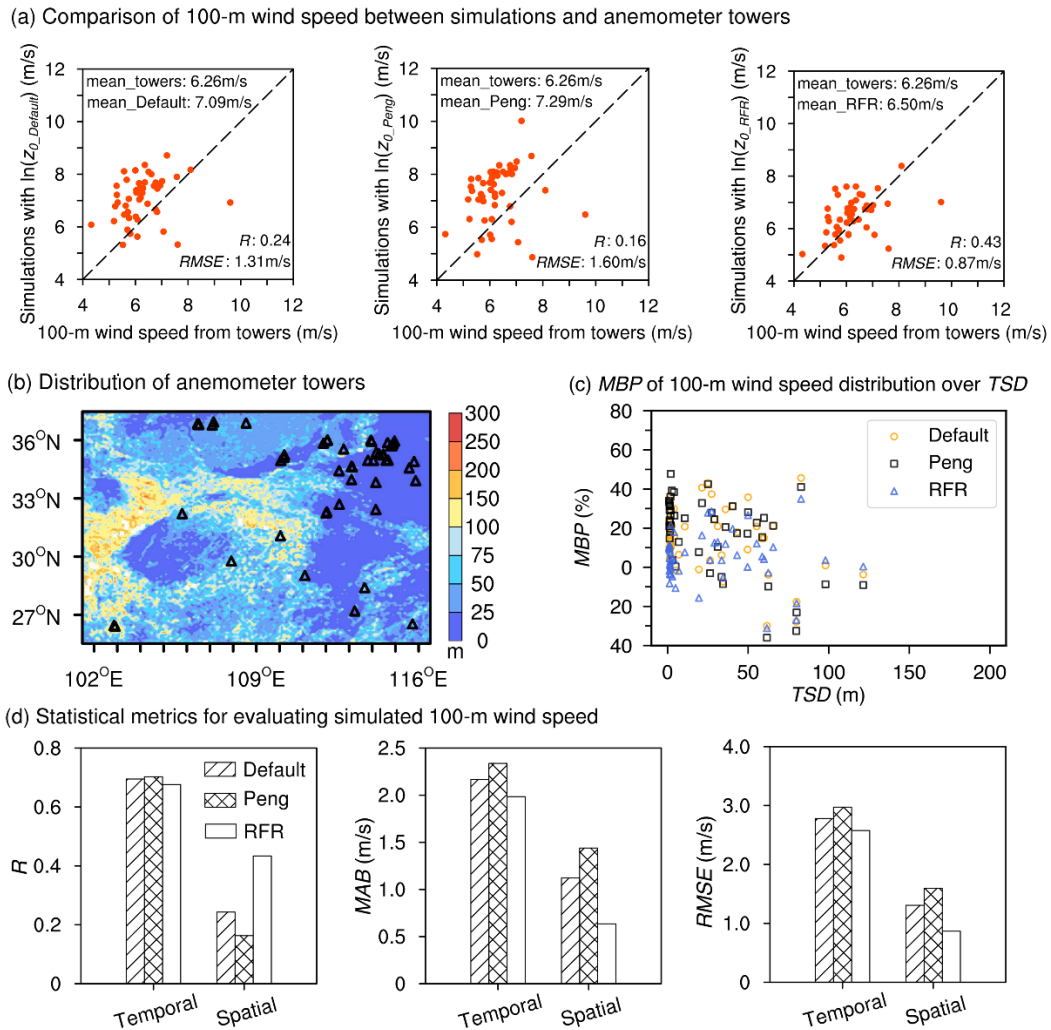


Figure 7. (a) Comparisons of mean 100-m wind speed in April between the simulations using $z_{0_Default}$, z_{0_Peng} , and z_{0_RFR} versus observations from anemometer towers. The corresponding wind speed means, R , and $RMSE$ of all towers are also indicated. (b) The locations of 50 anemometer towers (black triangles) utilized for 100-m wind speed evaluation. Colored shaded areas represent TSD . (c) Distribution of MBP in 100-m wind speed as a function of TSD . (d) Statistical metrics comparing simulated and observed 100-m wind speeds, including temporal and spatial R , MAB , and $RMSE$.

4. Discussion

Here we discuss the sensitivity and generality of the site z_0 estimation approach with respect to the input simulation or reanalysis data, addressing concerns about potential methodological dependence on ERA5. Our study utilized ERA5 reanalysis data and CMA observations for initial z_0 estimation. Compared to traditional meteorological or morphological

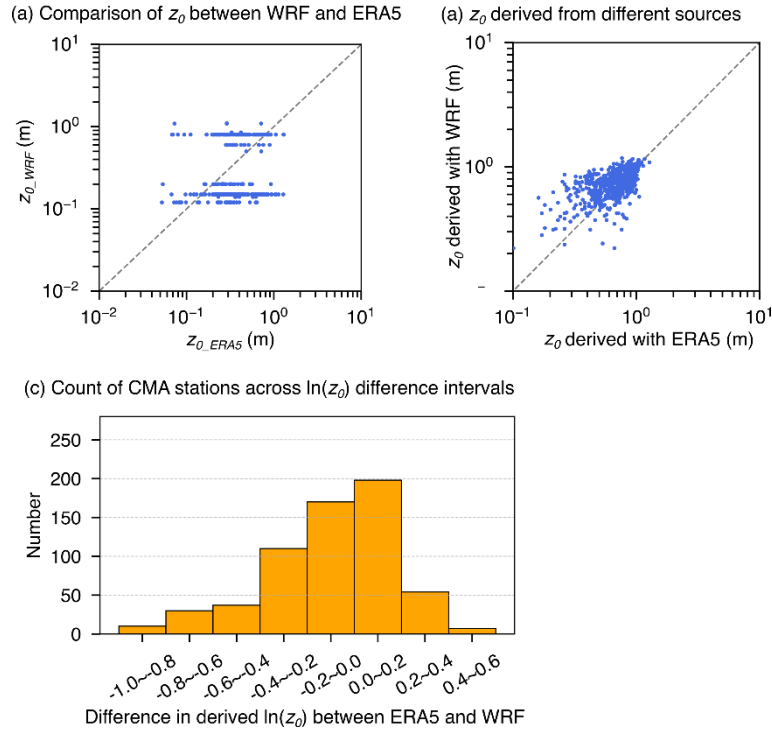
401 methods, our approach can provide z_0 values at large spatial coverage and low cost, and these values lead to clear
 402 improvements in WRF-simulated wind speeds at both 10 m and 100 m above ground level. To assess whether the
 403 performance gain stems from improved z_0 representation rather than from alignment with ERA5 reanalysis data, we carried
 404 out two additional sets of evaluations.

405 First, we applied the same approach to estimate z_0 from WRF-simulated 10-m wind speed and the model's default z_0 values
 406 ($0.03^\circ \times 0.03^\circ$), instead of ERA5. The z_0 values estimated using this alternative dataset were found to be highly similar to
 407 those derived from ERA5 (Fig. 8), indicating that the method is not inherently reliant on ERA5 as a data source. The primary
 408 advantage of using ERA5 lies in its extensive spatiotemporal coverage, which offers greater convenience and consistency
 409 with observational data. Meanwhile, although 10-m and 100-m winds over lands are not assimilated directly in ERA5, its
 410 4D-Var system ingests a wide range of surface and upper-air observations that constrain boundary-layer structure and
 411 indirectly improve near-surface winds; this strengthens the credibility of using ERA5 as the reference field (Hersbach et al.,
 412 2020). However, the methodology itself is general and transferable to other datasets.

413 Moreover, the agreement between ERA5- and WRF-derived z_0 values suggests that the spatial extent represented by the
 414 estimated site-level z_0 values is not determined by the resolution of the reanalysis or simulation dataset used, but rather by
 415 the measurement height of wind observations at the stations. In this study, 10-m wind speeds from CMA stations were used.
 416 As a rule of thumb, the horizontal representativeness of wind measurements is approximately 10-100 times the measurement
 417 height. Therefore, z_0 values estimated from 10-m wind observations are reasonably representative at ~ 100 m-1 km scales,
 418 making the generation of 0.01° gridded z_0 datasets for use in mesoscale simulations both appropriate and justified, with no
 419 evident resolution dependence observed. We compared simulation results at different resolutions. Leveraging the nested
 420 modeling setup used in this study, the d01 domain with a 0.09° resolution was treated as the coarse-resolution simulation,
 421 while d02 at 0.03° served as the fine-resolution simulation. The results show that, even at the coarser resolution, our gridded
 422 z_0 dataset provides a clear advantage and substantially improves near-surface wind speed simulations (Fig. S8 and S9).
 423 However, for simulations at ~ 1 km resolution and finer, such as urban-scale wind modelling, our z_0 dataset cannot fully
 424 capture urban heterogeneity, because it did not incorporate key morphological parameters (e.g., building height and density)
 425 to distinguish between different urban forms. Therefore, an urban canopy model (UCM) would be a more appropriate choice.
 426 UCMs were conceived to operate at ~ 0.5 -1 km grid spacing to bridge mesoscale forecasting ($\sim 10^5$ m) with microscale
 427 transport/dispersion ($\sim 10^0$ m) models (Tewari et al., 2006; Chen et al., 2010), and they have been widely applied and
 428 validated in subsequent urban studies (Lian et al., 2018; Salamanca et al., 2018; Wang et al., 2021). Therefore, our z_0 data
 429 are suitable and effective for mesoscale simulations at kilometer-level resolutions.

430 Second, we further validated the robustness of the refined z_0 dataset (z_{0_RFR}) by conducting additional WRF simulations
 431 driven by the reanalysis from National Centers for Environmental Prediction (NCEP) instead of ERA5. These results (Fig.
 432 S10 and Table S1) still showed significant improvement in wind speed simulation performance when using z_{0_RFR} ,

433 consistent with those driven by ERA5. This cross-reanalysis consistency demonstrates that the benefits are attributable to the
 434 improved surface representation through z_{0_RFR} refinement, not simply tuning to match ERA5-driven wind fields.
 435 Taken together, these findings confirm that the z_0 estimation method proposed in this study is robust, flexible, and not
 436 dependent on alignment with a specific reanalysis dataset. It provides a practical framework for z_0 estimation that can be
 437 widely applied across different reanalysis/simulation datasets and observational data with consistent benefits. However, this
 438 method is limited in regions with sparse or no surface weather stations. Notably, these regions, such as western and northern
 439 China, are rich in wind resources and are key targets for wind energy development. Therefore, producing high-quality
 440 gridded z_0 datasets in these regions warrants further study by exploring alternative data sources, such as anemometer tower
 441 wind profiles, to supplement z_0 truth values (Wang et al., 2024).



442 **Figure 8.** (a) Comparison of z_0 values from default WRF model (z_{0_WRF}) and ERA5 (z_{0_ERA5}). (b) Comparison of z_0 estimates using
 443 different datasets. z_0 derived from WRF represents the estimated values based on WRF simulations (10-m wind speed and default z_0) and
 444 CMA station observations (10-m wind speed) during April 2019, while z_0 derived from ERA5 denotes the estimates obtained in this study
 445 using ERA5 reanalysis data in April. (c) Distribution of station counts across intervals of the difference in derived $\ln(z_0)$ ($\ln(z_0)$ derived
 446 from ERA5 minus $\ln(z_0)$ derived from WRF).
 447 The two assumptions used in the z_0 estimation are also discussed. Although these assumptions cannot be fully verified with
 448 the available data, they are pragmatically motivated and indirectly supported by the improved performance of wind-speed
 449 simulations using the resulting z_0 estimates. Assumption 1 posits that the near-surface wind-speed discrepancy between
 450

ERA5 reanalysis and CMA observations is dominated by z_0 and that the influence of z_0 weakens with height, making ERA5 winds at higher levels within the surface layer comparable to observations. This is partly supported by the spatial pattern of estimated z_0 (denser over eastern China, where 100-m wind-speed biases between ERA5 reanalysis and anemometer tower observations are smaller (Figs. 1c and 2a)) and by a sensitivity test on the reference height (Figs. S11a and S11c). When re-estimating annual-mean z_{0_CMA} at 150 m and 200 m, most stations show an absolute difference from the 100-m-based estimate below 0.2, indicating broad consistency across heights. A minority of stations exhibit slightly larger deviation, which may be influenced by local terrain complexity (Figs. S11b and S11d). Assumption 2 treats the effects of atmospheric stability on wind speed as effectively similar in ERA5 and at CMA sites, allowing us to omit explicit stability corrections in estimating z_{0_CMA} . This simplification enhances methodological consistency and computational efficiency, and it is indirectly supported by the validation of simulated winds. Moreover, prior work has shown that neutral log-law method can perform comparably to stability-corrected scheme for vertical interpolation in U.S. wind-resource assessments (Duplyakin et al., 2021), suggesting that such an approximate treatment seems feasible and a widely adopted simplification. Overall, although neither assumption can be fully verified with the presently available data, their practical applicability is evidenced by improved WRF wind-speed simulations. Future work, ideally leveraging multi-height wind profile observations and coincident stability metrics could further test these assumptions, yield more precise z_0 estimates.

5. Conclusion

The representation of z_0 in numerical models, typically determined by land cover types, may lead to significant uncertainties in wind speed simulations and predictions. Traditional methods for obtaining z_0 ground truth are mainly constrained by high costs. In this study, we proposed a low-cost z_0 estimation method, allowing the acquisition of z_0 values at routine weather stations.

Specifically, this approach leverages 10-m wind speed and z_0 values from ERA5 reanalysis data, along with observed 10-m wind speeds at CMA stations, to derive optimal z_0 at stations by minimizing the difference in 100-m wind speeds between reanalysis and observations. Here, the 100-m wind speed is expressed with 10-m wind speed and z_0 using similarity theory. Based on this approach, we derived z_0 values at 1,837 CMA stations out of a total of 2,161 stations. These stations are located in high-roughness surface regions, indicating the estimated z_0 values inherently include the effects of built-up and tall vegetation.

To validate the reliability and practicality of the estimation method, we utilized a Random Forest Regression algorithm, incorporating feature variables closely related to z_0 , to develop a monthly gridded z_0 dataset for high-roughness surface areas in China with a spatial resolution of $0.01^\circ \times 0.01^\circ$. The resulting $\ln(z_0)$ values mainly range from -1 to 0. Simulations with WRF model show that, compared to the default z_0 in WRF and a recent gridded z_0 dataset developed by Peng et al. (2022), the z_0 dataset constructed in this study has significantly improved the accuracy of near-surface wind speed simulations in high-roughness surface areas, particularly in relatively flat regions. Evaluations against weather station data

and anemometer tower data show simulations with the new z_0 dataset mitigates mean bias of 10-m wind speed by 79.8% and 78.0%, and mean bias of 100-m wind speed by 71.1% and 76.7%, respectively, compared to the default z_0 in WRF and the z_0 dataset from Peng et al. (2022).

In summary, this study developed a simple yet effective approach for correcting model z_0 , addressing the limitations of relying on empirical values assigned based on land cover types. The method shows particular effectiveness in z_0 correction for high-roughness surface areas and offers valuable support for wind field-dependent studies and applications.

Code and data availability.

- Code required to conduct the analyses herein is available at <https://doi.org/10.5281/zenodo.15108200> (Wang, 2025).

The datasets used in this study fall into two categories based on their accessibility:

1. Publicly Available Datasets (accessible via DOI/URL).

- The hourly wind speed data at 10 m and 100 m heights are obtained from the ERA5 reanalysis dataset (Hersbach et al., 2020), accessible at <https://doi.org/10.24381/cds.adbb2d47> (Hersbach et al., 2023b).
- For the gridded datasets of z_0 used in this study, z_{0_ERA5} (Hersbach et al., 2020) is available at <https://doi.org/10.24381/cds.fl7050d7> (Hersbach et al., 2023a), while z_{0_Peng} (Peng et al., 2022) can be acquired by contacting the corresponding authors.
- The initial and boundary conditions for the simulations are from the ERA5 dataset (Hersbach et al., 2020), which can be downloaded from <https://doi.org/10.24381/cds.adbb2d47> (Hersbach et al., 2023b) and <https://doi.org/10.24381/cds.bd0915c6> (Hersbach et al., 2023c).
- The digital elevation data, with a spatial resolution of 3 arc-seconds, are sourced from the Shuttle Radar Topography Mission (SRTM) and can be downloaded from <https://csidotinfo.wordpress.com/data/srtm-90m-digital-elevation-database-v4-1/> (Jarvis et al., 2008).
- The urban-rural classification data (Li, X. et al., 2023) are available at <https://doi.org/10.6084/m9.figshare.21716357.v6> (Li et al., 2022).
- The variance of the slope ($\overline{\theta^2}$) data can be obtained by contacting Zhou et al. (2018).
- The Leaf Area Index (LAI) data (Lin et al., 2023; Yuan et al., 2011) are accessible at <http://globalchange.bnu.edu.cn/research/laiv061> (Beijing Normal University Global Change Data Archive, 2022).
- The percent tree cover data (DiMiceli et al., 2022) can be obtained from <https://doi.org/10.5067/MODIS/MOD44B.061> and [https://search.earthdata.nasa.gov/search/granules?p=C2565805839-LPCLOUD&pg\[0\]\[v\]=f&pg\[0\]\[gsk\]=-start_date&q=MOD44B&tl=1733462795.688!3!!&lat=-0.140625](https://search.earthdata.nasa.gov/search/granules?p=C2565805839-LPCLOUD&pg[0][v]=f&pg[0][gsk]=-start_date&q=MOD44B&tl=1733462795.688!3!!&lat=-0.140625) (NASA EOSDIS, 2024a).
- The NDVI data (Didan, 2021) are available from <https://doi.org/10.5067/MODIS/MOD13A3.061> and [https://search.earthdata.nasa.gov/search/granules?p=C2327962326-LPCLOUD&pg\[0\]\[v\]=f&pg\[0\]\[gsk\]=-start_date&q=MOD13A3&tl=1732851935.718!3!!&lat=-0.140625](https://search.earthdata.nasa.gov/search/granules?p=C2327962326-LPCLOUD&pg[0][v]=f&pg[0][gsk]=-start_date&q=MOD13A3&tl=1732851935.718!3!!&lat=-0.140625) (NASA EOSDIS, 2024b).
- The NCEP forcing data (National Centers for Environmental Prediction/National Weather Service/NOAA/U.S. Department of Commerce, 2025) are available from <https://rda.ucar.edu/datasets/d083002/dataaccess/>.

2. Restricted Datasets. We would like to clarify that the meteorological station data from the China Meteorological Administration (CMA) and the anemometer tower data used in this study are not publicly accessible but can be accessed through the following way. Specifically:

- The data from anemometer towers are provided by China State Shipbuilding Corporation Haizhuang Windpower Co., Ltd., however, they are not accessible publicly because of their commercial interests. These data can be obtained by cooperation with the company.
- The hourly 10-m wind speed data at meteorological stations are from the China Meteorological Administration (CMA). In accordance with the data policy of China, these data record are not directly accessible for public download via a website. Nevertheless, individuals interested in obtaining detailed information about data acquisition can reach out to

the China Meteorological Data Service Center at their official website
(<http://data.cma.cn/en/?r=data/detail&dataCode=A.0012.0001>, China meteorological data service centre, 2023).

Author contributions. All authors contributed to the study. JW and KY conceived the study and conducted the design; JW, KY, and JL carried out data analyses; JW, XZ and XM performed the configuration of WRF model; WT processed data from CMA stations; LY provided the data from anemometer towers; ZR conducted data collection and cleaning of anemometer towers; JW and KY wrote the manuscript; all authors discussed, reviewed and edited the manuscript.

Competing interests. The contact author has declared that none of the authors has any competing interests.

Disclaimer. Publisher's note: Copernicus Publications remains neutral with regard to jurisdictional claims in published maps and institutional affiliations.

Financial support. This work was supported by the National Natural Science Foundation of China (Grant Nos. 42475138 and 42361144875) and Huadian Xizang Energy Co., Ltd. (Grant No. 12IJD202400023).

References

- Beljaars, A., Brown, A. R. and Wood, N: A new parametrization of turbulent orographic form drag, Q. J. R. Meteorol. Soc., 130, 1327-1347, doi:10.1256/qj.03.73, 2010.
- Beijing Normal University Global Change Data Archive: Leaf Area Index (LAI) Dataset [data set], <http://globalchange.bnu.edu.cn/research/laiv061>, last access: 24 March 2022.
- Breiman, L.: Random forests, Mach. Learn., 45, 5-32, doi:10.1023/A:1010933404324, 2001.
- Bottema, M. and Mestayer, P. G.: Urban roughness mapping - Validation techniques and some first results, J. Wind Eng. Ind. Aerodyn., 74-76, 163-173, doi:10.1016/S0167-6105(98)00014-2, 1998.
- Chen, F., Kusaka, H., Bornstein, R., Ching, J., Grimmond, C. S. B., Grossman-Clarke, S., Loridan, T., Manning, K. W., Martilli, A., Miao, S., Sailor, D., Salamanca, F. P., Taha, H., Tewari, M., Wang, X., Wyszogrodzki, A. A., and Zhang, C.: The integrated WRF/urban modelling system: development, evaluation, and applications to urban environmental problems, Int. J. Climatol., 31, 273-288, doi:10.1002/joc.2158, 2011.
- China meteorological data service centre: Daily Timed Data from automated weather stations in China [data set], <http://data.cma.cn/en/?r=data/detail&dataCode=A.0012.0001>, last access: 6 May 2023.
- Danielson, J. J., and Gesch, D. B.: Global multi-resolution terrain elevation data 2010 (GMTED2010), US Geological Survey, No. 2011-1073, doi:10.3133/ofr20111073, 2011.
- Di Nicola, F., Brattich, E. and Di Sabatino, S.: A new approach for roughness representation within urban dispersion models, Atmos. Environ., 283, 119181, doi:10.1016/j.atmosenv.2022.119181, 2022.

561 Didan, K.: MODIS/Terra Vegetation Indices Monthly L3 Global 1km SIN Grid V061, NASA EOSDIS Land Processes
562 Distributed Active Archive Center [data set], doi:10.5067/MODIS/MOD13A3.061.

563 DiMiceli, C., Sohlberg, R. and Townshend, J.: MODIS/Terra Vegetation Continuous Fields Yearly L3 Global 250m SIN
564 Grid V061, NASA EOSDIS Land Processes Distributed Active Archive Center [data set],
565 doi:10.5067/MODIS/MOD44B.061, 2022.

566 Draxl, C., Worsnop, R. P., Xia, G., Pichugina, Y., Chand, D., Lundquist, J. K., Sharp, J., Wedam, G., Wilczak, J. M., and
567 Berg, L. K.: Mountain waves can impact wind power generation, *Wind Energ. Sci.*, 6, 45-60, doi:10.5194/wes-6-45-2021,
568 2021.

569 Duan, G. and Takemi, T.: Predicting urban surface roughness aerodynamic parameters using random forest, *J. Appl.*
570 *Meteorol. Climatol.*, 60, 999-1018, doi:10.1175/JAMC-D-20-0266.1, 2021.

571 Dudhia, J.: Numerical study of convection observed during the winter monsoon experiment using a mesoscale two-
572 dimensional model, *J. Atmos. Sci.*, 46, 3077-3107, doi:10.1175/1520-0469(1989)046<3077:NSOCOD>2.0.CO;2, 1989.

573 Duplyakin, D., Zisman, S., Phillips, C., and Tinnensand, H.: Bias characterization, vertical interpolation, and horizontal
574 interpolation for distributed wind siting using mesoscale wind resource estimates, National Renewable Energy Laboratory
575 (NREL), Golden, CO, USA, NREL/TP-2C00-78412, doi:10.2172/1760659, 2021.

576 Ge, C., Yan, J., Song, W., Zhang, H., Wang, H., Li, Y. and Liu, Y.: Middle-term wind power forecasting method based on
577 long-span NWP and microscale terrain fusion correction, *Renew. Energy*, 240, 122123, doi:10.1016/j.renene.2024.122123,
578 2025.

579 Grell, G. A. and Freitas, S. R.: A scale and aerosol aware stochastic convective parameterization for weather and air quality
580 modeling, *Atmos. Chem. Phys.*, 14, 5233-5250, doi:10.5194/acpd-13-23845-2013, 2014.

581 Grimmond, C. S. B., King, T. S., Roth, M. and Oke, T. R.: Aerodynamic roughness of urban areas derived from wind
582 observations, *Bound.-Layer Meteorol.*, 89, 1-24, doi:10.1023/A:1001525622213, 1998.

583 Grimmond, C. S. B. and Oke, T. R.: Aerodynamic properties of urban areas derived from analysis of surface form, *J. Appl.*
584 *Meteorol. Climatol.*, 38, 1262-1292, doi:10.1175/1520-0450(1999)038<1262:APOUAD>2.0.CO;2, 1999.

585 Hadavi, M. and Pasharshahri, H.: Quantifying impacts of wind speed and urban neighborhood layout on the infiltration rate
586 of residential buildings, *Sustain. Cities Soc.*, 53, 101887, doi:10.1016/j.scs.2019.101887, 2020.

587 Han, Z., Zhou, B., Xu, Y., Wu, J. and Shi, Y.: Projected changes in haze pollution potential in China: an ensemble of
588 regional climate model simulations, *Atmos. Chem. Phys.*, 17, 10109-10123, doi:10.5194/acp-17-10109-2017, 2017.

589 Hersbach, H., Bell, B., Berrisford, P., Biavati, G., Horányi, A., Muñoz Sabater, J., Nicolas, J., Peubey, C., Radu, R., Rozum,
590 I., Schepers, D., Simmons, A., Soci, C., Dee, D. and Thépaut, J.-N.: ERA5 monthly averaged data on single levels from 1940
591 to present, Copernicus Climate Change Service (C3S) Climate Data Store (CDS) [data set], doi:10.24381/cds.f17050d7,
592 2023a.

593 Hersbach, H., Bell, B., Berrisford, P., Biavati, G., Horányi, A., Muñoz Sabater, J., Nicolas, J., Peubey, C., Radu, R., Rozum,
 594 I., Schepers, D., Simmons, A., Soci, C., Dee, D. and Thépaut, J.-N.: ERA5 hourly data on single levels from 1940 to present,
 595 Copernicus Climate Change Service (C3S) Climate Data Store (CDS) [data set], doi:10.24381/cds.adbb2d47, 2023b.
 596 Hersbach, H., Bell, B., Berrisford, P., Biavati, G., Horányi, A., Muñoz Sabater, J., et al.: ERA5 hourly data on pressure
 597 levels from 1940 to present, Copernicus Climate Change Service (C3S) Climate Data Store (CDS) [data set],
 598 doi:10.24381/cds.bd0915c6, 2023c.
 599 Hersbach, H., Bell, B., Berrisford, P., Hirahara, S., Horányi, A., Muñoz-Sabater, J., Nicolas, J., Peubey, C., Radu, R.,
 600 Schepers, D., Simmons, A., Soci, C., Abdalla, S., Abellan, X., Balsamo, G., Bechtold, P., Biavati, G., Bidlot, J., Bonavita,
 601 M., De Chiara, G., Dahlgren, P., Dee, D., Diamantakis, M., Dragani, R., Flemming, J., Forbes, R., Fuentes, M., Geer, A.,
 602 Haimberger, L., Healy, S., Hogan, R. J., Hólm, E., Janisková, M., Keeley, S., Laloyaux, P., Lopez, P., Lupu, C., Radnoti, G.,
 603 de Rosnay, P., Rozum, I., Vamborg, F., Villaume, S., and Thépaut, J.-N.: The ERA5 global reanalysis, *Q. J. R. Meteorol.*
 604 *Soc.*, 146, 1999-2049, doi:10.1002/qj.3803, 2020.
 605 Hong, S. Y., Noh, Y. and Dudhia, J.: A new vertical diffusion package with an explicit treatment of entrainment processes,
 606 *Mon. Weather Rev.*, 134, 2318-2341, doi:10.1175/MWR3199.1, 2006.
 607 Hu, X., Shi, L., Lin, L. and Magliulo, V.: Improving surface roughness lengths estimation using machine learning algorithms,
 608 *Agric. For. Meteorol.*, 287, 107956, doi:10.1016/j.agrformet.2020.107956, 2020.
 609 Ishugah, T. F., Li, Y., Wang, R. Z. and Kiplagat, J. K.: Advances in wind energy resource exploitation in urban environment:
 610 A review, *Renew. Sustain. Energy Rev.*, 37, 613-626, doi:10.1016/j.rser.2014.05.053, 2014.
 611 Jarvis, A., Reuter, H. I., Nelson, A. and Guevara, E.: Hole-filled SRTM for the globe Version 4, CGIAR-CSI SRTM 90m
 612 Database [data set], <http://srtm.csi.cgiar.org>, 2008.
 613 Jiménez, P. A. and Dudhia, J.: Improving the representation of resolved and unresolved topographic effects on surface wind
 614 in the WRF model, *J. Appl. Meteorol. Climatol.*, 51, 300-316, doi:10.1175/JAMC-D-11-084.1, 2012.
 615 Kammen, D. M. and Sunter, D. A.: City-integrated renewable energy for urban sustainability, *Science*, 352, 922-928,
 616 doi:10.1126/science.aad9302, 2016.
 617 Kanda, M., Inagaki, A., Miyamoto, T., Gryschka, M. and Raasch, S.: A new aerodynamic parametrization for real urban
 618 surfaces, *Bound.-Layer Meteorol.*, 148, 357-377, doi:10.1007/s10546-013-9818-x, 2013.
 619 Kim, G., Lee, J., Lee, M. I. and Kim, D.: Impacts of urbanization on atmospheric circulation and aerosol transport in a
 620 coastal environment simulated by the WRF-Chem coupled with urban canopy model, *Atmos. Environ.*, 249, 118253,
 621 doi:10.1016/j.atmosenv.2021.118253, 2021.
 622 Li, Z., Song, L., Ma, H., Xiao, J., Wang, K. and Chen, L.: Observed surface wind speed declining induced by urbanization in
 623 East China, *Clim. Dyn.*, 50, 735-749, doi:10.1007/s00382-017-3637-6, 2018.
 624 Li, D., Liao, W., Rigden, A. J., Liu, X., Wang, D., Malyshev, S. and Shevliakova, E.: Urban heat island: Aerodynamics or
 625 imperviousness?, *Sci. Adv.*, 5, eaau4299, doi:10.1126/sciadv.aau4299, 2019.

626 Li, X., Yu, L. and Chen, X.: New insights into urbanization based on global mapping and analysis of human settlements in
627 the rural-urban continuum, *Land*, 12, 1607, doi:10.3390/land12081607, 2023.

628 Li, X., Yu, L. and Chen, X.: New insights into urbanization based on global mapping and analysis of human settlements in
629 the rural-urban continuum [data set]. figshare. doi:10.6084/m9.figshare.21716357.v6, 2022.

630 Li, Y., Sun, P. P., Li, A. and Deng, Y.: Wind effect analysis of a high-rise ancient wooden tower with a particular
631 architectural profile via wind tunnel test, *Int. J. Archit. Herit.*, 17, 518-537, doi:10.1080/15583058.2021.1938748, 2023.

632 Lian, J., Wu, L., Bréon, F.-M., Broquet, G., Vautard, R., Zaccheo, T. S., Dobler, J., and Ciais, P.: Evaluation of the WRF-
633 UCM mesoscale model and ECMWF global operational forecasts over the Paris region in the prospect of tracer atmospheric
634 transport modeling, *Elem. Sci. Anth.*, 6, 64, doi:10.1525/elementa.319, 2018.

635 Lin, W., Yuan, H., Dong, W., Zhang, S., Liu, S., Wei, N., Lu, X., Wei, Z., Hu, Y. and Dai, Y.: Reprocessed MODIS version
636 6.1 leaf area index dataset and its evaluation for land surface and climate modeling, *Remote Sens.*, 15, 1780,
637 doi:10.3390/rs15071780, 2023.

638 Liu, J., Gao, Z., Wang, L., Li, Y. and Gao, C. Y.: The impact of urbanization on wind speed and surface aerodynamic
639 characteristics in Beijing during 1991-2011, *Meteorol. Atmos. Phys.*, 130, 311-324, doi:10.1007/s00703-017-0519-8, 2018.

640 Liu, Z., He, C., Zhou, Y. and Wu, J.: How much of the world's land has been urbanized, really? A hierarchical framework
641 for avoiding confusion, *Landsc. Ecol.*, 29, 763-771, doi:10.1007/s10980-014-0034-y, 2014.

642 Luu, L. N., van Meijgaard, E., Philip, S. Y., Kew, S. F., de Baar, J. H. S. and Stepek, A.: Impact of surface roughness
643 changes on surface wind speed over western Europe: A study with the regional climate model RACMO, *J. Geophys. Res.-*
644 *Atmos.*, 128, e2022JD038426, doi:10.1029/2022JD038426, 2023.

645 Macdonald, R. W., Griffiths, R. F. and Hall, D. J.: An improved method for the estimation of surface roughness of obstacle
646 arrays, *Atmos. Environ.*, 32, 1857-1864, doi:10.1016/S1352-2310(97)00403-2, 1998.

647 Manju, N., Balakrishnan, R. and Mani, N.: Assimilative capacity and pollutant dispersion studies for the industrial zone of
648 Manali, *Atmos. Environ.*, 36, 3461-3471, doi:10.1016/S1352-2310(02)00306-0, 2002.

649 Mlawer, E. J., Taubman, S. J., Brown, P. D., Iacono, M. J. and Clough, S. A.: Radiative transfer for inhomogeneous
650 atmospheres: RRTM, a validated correlated-k model for the longwave, *J. Geophys. Res.*, 102, 16663-16682,
651 doi:10.1029/97JD00237, 1997.

652 Monin, A. S. and Obukhov, A. M.: Osnovnye zakonomernosti turbulentnogo peremesivaniya v prizemnon sloe atmosfery
653 (Basic laws of turbulent mixing in the atmosphere near the ground), *Dokl. Akad. Nauk SSSR*, 151, 1963-1987, 1954.

654 NASA EOSDIS: MODIS/Terra Vegetation Continuous Fields Yearly L3 Global 250m SIN Grid V061 [data set],
655 [https://search.earthdata.nasa.gov/search/granules?p=C2565805839-LPCLOUD&pg\[0\]\[v\]=f&pg\[0\]\[gsk\]=-](https://search.earthdata.nasa.gov/search/granules?p=C2565805839-LPCLOUD&pg[0][v]=f&pg[0][gsk]=-start_date&q=MOD44B&tl=1733462795.688!3!!&lat=-0.140625)
656 [start_date&q=MOD44B&tl=1733462795.688!3!!&lat=-0.140625](https://search.earthdata.nasa.gov/search/granules?p=C2565805839-LPCLOUD&pg[0][v]=f&pg[0][gsk]=-start_date&q=MOD44B&tl=1733462795.688!3!!&lat=-0.140625), last access: 3 October 2024a.

657 NASA EOSDIS: MODIS/Terra Vegetation Indices Monthly L3 Global 1km SIN Grid V061 [data set],
658 [https://search.earthdata.nasa.gov/search/granules?p=C2327962326-LPCLOUD&pg\[0\]\[v\]=f&pg\[0\]\[gsk\]=-](https://search.earthdata.nasa.gov/search/granules?p=C2327962326-LPCLOUD&pg[0][v]=f&pg[0][gsk]=-start_date&q=MOD13A3&tl=1732851935.718!3!!&lat=-0.140625)
659 [start_date&q=MOD13A3&tl=1732851935.718!3!!&lat=-0.140625](https://search.earthdata.nasa.gov/search/granules?p=C2327962326-LPCLOUD&pg[0][v]=f&pg[0][gsk]=-start_date&q=MOD13A3&tl=1732851935.718!3!!&lat=-0.140625), last access: 22 September 2024b.

660 National Centers for Environmental Prediction/National Weather Service/NOAA/U.S. Department of Commerce. 2000,
661 updated daily. *NCEP FNL Operational Model Global Tropospheric Analyses, continuing from July 1999* [data set]. Research
662 Data Archive at the National Center for Atmospheric Research, Computational and Information Systems Laboratory.
663 <https://doi.org/10.5065/D6M043C6>. Accessed 28 May 2025.

664 Niu, G. Y., Yang, Z. L. and Mitchell, K. E.: The community Noah land surface model with multiparameterization options
665 (Noah-MP): 1. Model description and evaluation with local-scale measurements, *J. Geophys. Res.-Atmos.*, 116, D12109,
666 doi:10.1029/2010JD015139, 2011.

667 Peng, Z., Tang, R., Jiang, Y., Liu, M. and Li, Z. L.: Global estimates of 500 m daily aerodynamic roughness length from
668 MODIS data, *ISPRS J. Photogramm. Remote Sens.*, 183, 336-351, doi:10.1016/j.isprsjprs.2021.11.015, 2022.

669 Peng, Z., Tang, R., Liu, M., Jiang, Y. and Li, Z. L.: Coupled estimation of global 500m daily aerodynamic roughness length,
670 zero-plane displacement height and canopy height, *Agric. For. Meteorol.*, 342, 109754,
671 doi:10.1016/j.agrformet.2023.109754, 2023.

672 Raupach, M. R.: Drag and drag partition on rough surfaces, *Bound.-Layer Meteorol.*, 60, 375-395, doi:10.1007/BF00155203,
673 1992.

674 Raupach, M. R.: Simplified expressions for vegetation roughness length and zero-plane displacement as functions of canopy
675 height and area index, *Bound.-Layer Meteorol.*, 71, 211-216, doi:10.1007/BF00709229, 1994.

676 Roy, P., Chen, L. W. A., Chen, Y. T., Ahmad, S., Khan, E. and Buttner, M.: Pollen dispersion and deposition in real-world
677 urban settings: A computational fluid dynamic study, *Aerosol Sci. Eng.*, 7, 543-555, doi:10.1007/s41810-023-00198-1, 2023.

678 Salamanca, F., Zhang, Y., Barlage, M., Chen, F., Mahalov, A., and Miao, S.: Evaluation of the WRF-urban modeling system
679 coupled to Noah and Noah-MP land surface models over a semiarid urban environment, *J. Geophys. Res.-Atmos.*, 123,
680 2387-2408, doi:10.1002/2018JD028377, 2018.

681 Shen, C., Shen, A., Cui, Y., Chen, X., Liu, Y., Fan, Q., Chan, P., Tian, C., Wang, C., Lan, J., Gao, M., Li, X. and Wu, J.:
682 Spatializing the roughness length of heterogeneous urban underlying surfaces to improve the WRF simulation-part 1: A
683 review of morphological methods and model evaluation, *Atmos. Environ.*, 270, 118874,
684 doi:10.1016/j.atmosenv.2021.118874, 2022.

685 Shen, G., Zheng, S., Jiang, Y., Zhou, W. and Zhu, D.: An improved method for calculating urban ground roughness
686 considering the length and angle of upwind sector, *Build. Environ.*, 266, 112144, doi:10.1016/j.buildenv.2024.112144, 2024.

687 Skamarock, W. C., Klemp, J. B., Dudhia, J., Gill, D. O., Liu, Z., Berner, J., Wang, W., Powers, J. G., Duda, M. G., Barker,
688 D. M. and Huang, X.-Y.: A description of the advanced research WRF model version 4 Rep (Vol. 145). National Center for
689 Atmos Res National Center for Atmospheric Research. doi:10.5065/1DFH-6P97, 2019.

690 Stathopoulos, T., Alrawashdeh, H., Al-Quraan, A., Blocken, B., Dilimulati, A., Paraschivoiu, M. and Pilay, P.: Urban wind
691 energy: Some views on potential and challenges, *J. Wind Eng. Ind. Aerodyn.*, 179, 146-157,
692 doi:10.1016/j.jweia.2018.05.018, 2018.

693 Stull, R. B.: An introduction to boundary layer meteorology, Springer Science & Business Media, 1988.

694 Tanentzap, A. J., Taylor, P. A., Yan, N. D., and Salmon, J. R.: On Sudbury-area wind speeds—a tale of forest regeneration.
695 *Journal of applied meteorology and climatology*, 46(10), 1645-1654, doi:10.1175/JAM2552.1, 2007.

696 Tasneem, Z., Noman, A. A., Das, S. K., Saha, D. K., Islam, M. R., Ali, M. F., Badal, M. F. R., Ahamed, M. H., Moyeen, S. I.
697 and Alam, F.: An analytical review on the evaluation of wind resource and wind turbine for urban application: Prospect and
698 challenges, *Dev. Built Environ.*, 4, 100033, doi:10.1016/j.dibe.2020.100033, 2020.

699 Tewari, M., Chen, F., and Kusaka, H.: Implementation and evaluation of a single-layer urban canopy model in WRF/Noah,
700 In: *Proceedings of the WRF Users' Workshop*, NCAR, Boulder, CO, USA, 2006.

701 Thompson, G., Field, P. R., Rasmussen, R. M. and Hall, W. D.: Explicit forecasts of winter precipitation using an improved
702 bulk microphysics scheme. Part II: implementation of a new snow parameterization, *Mon. Weather Rev.*, 136, 5095-5115,
703 doi:10.1175/2008MWR2387.1, 2008.

704 Wang, J.: Codes for manuscript “Improvement of near-surface wind speed modeling through refined aerodynamic roughness
705 length in high-roughness surface regions: implementation and validation in the Weather Research and Forecasting (WRF)
706 model version 4.0”, Zenodo [code], doi: 10.5281/zenodo.15108200, 2025.

707 Wang, J. and Hu, X.-M.: Evaluating the performance of WRF urban schemes and PBL schemes over Dallas-Fort Worth
708 during a dry summer and a wet summer, *J. Appl. Meteorol. Climatol.*, 60, 779-798, doi:10.1175/JAMC-D-19-0195.1, 2021.

709 Wang, J., Yang, K., Yuan, L., Liu, J., Peng, Z., Ren, Z. and Zhou, X.: Deducing aerodynamic roughness length from
710 abundant anemometer tower data to inform wind resource modeling, *Geophys. Res. Lett.*, 51, e2024GL111056,
711 doi:10.1029/2024GL111056, 2024.

712 Watts, C. J., Chehbouni, A., Rodriguez, J. C., Kerr, Y. H., Hartogensis, O. and de Bruin, H. A. R.: Comparison of sensible
713 heat flux estimates using AVHRR with scintillometer measurements over semi-arid grassland in northwest Mexico, *Agric.*
714 *For. Meteorol.*, 105, 81-89, doi:10.1016/S0168-1923(00)00188-X, 2000.

715 Wever, N.: Quantifying trends in surface roughness and the effect on surface wind speed observations, *J. Geophys. Res.-*
716 *Atmos.*, 117, D11101, doi:10.1029/2011JD017118, 2012.

717 Wieringa, J.: Representative roughness parameters for homogeneous terrain, *Bound.-Layer Meteorol.*, 63, 323-363, 1993.

718 Winckler, J., Reick, C. H., Bright, R. M. and Pongratz, J.: Importance of surface roughness for the local biogeophysical
719 effects of deforestation, *J. Geophys. Res.-Atmos.*, 124, 8605-8618, doi:10.1029/2018JD030127, 2019.

720 Wong, C. C. and Liu, C. H.: Pollutant plume dispersion in the atmospheric boundary layer over idealized urban roughness,
721 *Bound.-Layer Meteorol.*, 147, 281-300, doi:10.1007/s10546-012-9785-7, 2013.

722 Wu, J., Zha, J., Zhao, D. and Yang, Q.: Effects of surface friction and turbulent mixing on long-term changes in the near-
723 surface wind speed over the eastern China plain from 1981 to 2010, *Clim. Dynam.*, 51, 1-15, doi:10.1007/s00382-017-4012-
724 3, 2017.

725 Yuan, H., Dai, Y., Xiao, Z., Ji, D. and Shanguan, W.: Reprocessing the MODIS leaf area index products for land surface
726 and climate modelling, *Remote Sens. Environ.*, 115, 1171-1187, doi:10.1016/j.rse.2011.01.001, 2011.

727 Zhang, F., Sha, M., Wang, G., Li, Z. and Shao, Y.: Urban aerodynamic roughness length mapping using multitemporal SAR
728 data, *Adv. Meteorol.*, 2017, 8958926, doi:10.1155/2017/8958926, 2017.

729 Zhang, Z., Wang, K., Chen, D., Li, J. and Robert, D.: Increase in surface friction dominates the observed surface wind speed
730 decline during 1973-2014 in the northern hemisphere lands, *J. Climate*, 32, 7421-7435, doi:10.1175/JCLI-D-18-0691.1, 2019.

731 Zhang, Z. and Wang, K.: Quantifying and adjusting the impact of urbanization on the observed surface wind speed over
732 China from 1985 to 2017, *Fundam. Res.*, 1, 785-791, doi:10.1016/j.fmre.2021.09.006, 2021.

733 Zhao, L., Lee, X., Smith, R. B. and Oleson, K.: Strong contributions of local background climate to urban heat islands,
734 *Nature*, 511, 216-219, doi:10.1038/nature13462, 2014.

735 Zhou, X., Yang, K. and Wang, Y.: Implementation of a turbulent orographic form drag scheme in WRF and its application to
736 the Tibetan Plateau, *Clim. Dynam.*, 50, 2443-2455, doi:10.1007/s00382-017-3677-y, 2018.